CORONAVIRUS

Pharmacological modulators of epithelial immunity uncovered by synthetic genetic tracing of SARS-CoV-2 infection responses

Ben Jiang[1]†, Matthias Jürgen Schmitt[1]†, Ulfert Rand[2], Carlos Company[1], Yuliia Dramaretska[1], Melanie Grossmann[1], Michela Serresi[1], Luka Čičin-Šain[2], Gaetano Gargiulo[1]*

Epithelial immune responses govern tissue homeostasis and offer drug targets against maladaptation. Here, we report a framework to generate drug discovery–ready reporters of cellular responses to viral infection. We reverse-engineered epithelial cell responses to SARS-CoV-2, the viral agent fueling the ongoing COVID-19 pandemic, and designed synthetic transcriptional reporters whose molecular logic comprises interferon-α/β/γ and NF-κB pathways. Such regulatory potential reflected single-cell data from experimental models to severe COVID-19 patient epithelial cells infected by SARS-CoV-2. SARS-CoV-2, type I interferons, and RIG-I drive reporter activation. Live-cell image–based phenotypic drug screens identified JAK inhibitors and DNA damage inducers as antagonistic modulators of epithelial cell response to interferons, RIG-I stimulation, and SARS-CoV-2. Synergistic or antagonistic modulation of the reporter by drugs underscored their mechanism of action and convergence on endogenous transcriptional programs. Our study describes a tool for dissecting antiviral responses to infection and sterile cues and rapidly discovering rational drug combinations for emerging viruses of concern.

INTRODUCTION

Severe acute respiratory syndrome coronavirus 2 (SARS-CoV-2) is the etiological agent of the coronavirus disease 2019 (COVID-19) pandemic, which caused the death or long-term illness of millions of people while simultaneously imposing severe social and economic burden worldwide. COVID-19 is currently managed through massive vaccination, notably with the aid of novel mRNA vaccines (*1*). However, SARS-CoV-2 displayed remarkable evolutionary potential and multiple strains emerged over the past 2 years, with the Omicron variant currently being the dominant strain globally. Immunity against SARS-CoV-2 strains is limited and continuously threatened by emerging variants (*1*).

Pharmacological treatments that reduce the risk of progression in COVID-19 patients are imperfect, and their efficacy is restricted to the early intervention (*2*–*5*). In particular, the direct intervention through antiviral drugs has been generally underwhelming, and the currently approved orally bioavailable prodrug of N4-hydroxycytidine (molnupiravir) showed modest efficacy in a placebo-controlled phase 2/3 trial (*2*), indicating that combination therapies will be required to effectively control disease progression.

One preferential entry site for SARS-CoV-2 is the nasal cavity, where the cells located in the upper respiratory tract, such as the nasal epithelial cells and alveolar epithelial type II cells, are targeted by the virus. Both share high coexpression of ACE2 and TMPRSS2, the putative main receptor and surface protease, respectively, mediating the entry of the several SARS-CoV-2 strains (*6*). SARS-CoV-2 infection leads to transcriptional changes associated with innate immune response in the epithelial cells, including chemokine secretion (*7*), which is believed to trigger a cascade of proinflammatory innate immune cell recruitment (macrophages and neutrophils) and disease progression (*7*). Therefore, the first line of defense against SARS-CoV-2 infection is the innate immune system of the upper respiratory tract epithelial cells. One key step of the epithelial cells innate immune response is the production of type I interferons (IFNs), which induce an antiviral state in neighboring cells and trigger the activation of the adaptive immune system to protect the host against viral infection. SARS-CoV-2 elicits activation of pattern recognition receptors (PRRs), such as cytoplasmic RIG-I/MDA5 (*8*) as well as Toll-like receptor 2 (TLR2) (*9*) and several other TLRs (*10*). Upon binding to the viral nucleic acids, PRRs activate the nuclear translocation of two families of transcription factors (TFs), notably the IFN regulatory factors (IRFs), such as *IRF3* and *IRF7*, and the nuclear factor κB (*NF-κB*) factors *p65* and *p50*, which coordinate the antiviral and acute inflammatory cellular responses (*11*). One of the subsequent interconnected events is the transcription of IFN genes, which in turn are secreted and engage the type I IFN receptors (e.g., IFNAR1 and IFNAR2). IFN activation of the Janus kinase/signal transducer and activator of transcription (JAK/STAT) signaling pathway in both infected and neighbor cells leads to the transcription of IFN-stimulated gene (ISG) signaling that builds up an antiviral state in the cell (*6*). To counteract host cell responses, viruses hijack the activation of the IFN pathway, limit the active antiviral response, and inhibit antiviral signaling (*12*). This leads to the coexistence of viral replication and viral antagonism within the infected cell population. Hence, the transcriptional response of epithelial cells is one of the key events that inform on viral infection. Moreover, innate immunity can be activated or amplified by several other pathways, including purely sterile inflammatory environmental triggers, such as DNA damage inducers (*13*).

The pathways controlling the transcriptional response of epithelial cells to infection offer an outstanding opportunity for intervention. Whereas drugs with different mechanisms of action targeting

[1]Max-Delbrück-Center for Molecular Medicine (MDC), Robert-Rössle-Str. 10, 13092 Berlin, Germany. [2]Helmholtz-Zentrum für Infektionsforschung GmbH (HZI), Inhoffenstraße 7, 38124 Braunschweig, Germany.
*Corresponding author. Email: gaetano.gargiulo@mdc-berlin.de
†These authors contributed equally to this work.

the key nodes of the PRRs, NF-κB, and JAK/STAT pathways are available and offer an opportunity for creating combination therapies, there is lack in technologies to rationally design combination treatments with synergistic antiviral activity and less prone to resistance. Furthermore, phenotypic drug discovery platforms to identify novel drugs and combinations thereof are potential game changers (*14*), but there are limited phenotypic readouts for SARS-CoV-2 infection, and RNA viruses in general. Recently, we developed a method to generate synthetic locus control regions (sLCRs) to enable genetic tracing of complex phenotypes, including inflammatory transcriptional responses (*15*, *16*). Using an evolved computational approach to design phenotype-specific sLCRs named logical design of synthetic cis-regulatory DNA [LSD (*17*)], we generate sLCRs designed to intercept the transcriptional response of epithelial cells to SARS-CoV-2 infection using the earliest publicly available signatures in cell models (*18*–*20*). We characterized one reporter for genetic tracing of cellular response to SARS-CoV-2, which represents cell states including those described in upper airway tracts of severe COVID-19 patients (*7*). This sLCR responds to cellular stimulation by the IFN pathway and of the PRRs. Hence, it is serving as a platform for unbiased drug discovery of synergistic modulators of epithelial immune responses from viral and sterile triggers and to study their mechanism of action.

RESULTS

Designing sLCRs for SARS-CoV-2 productive infection in epithelial cells

To design SARS-CoV-2 reporters that would model infection response in epithelial cells, we first defined the input for LSD, namely, SARS-CoV-2 signature and TF genes (Fig. 1A). We overlaid bulk and single-cell gene expression data from the earliest available reports in lung epithelial cells overexpressing the ACE2 SARS-CoV-2 entry receptor [A549 + ACE2 (*18*)] and endogenously expressing ACE2 and the preferential SARS-CoV-2 protease TMPSSR2 [Calu-3 (*18*)], as well as from primary gastrointestinal organoids (*19*). In response to SARS-CoV-2 infection, each cell type expressed private and shared genes between 12 and 60 hours post-infection (hpi), and we selected signature and TF genes that were up-regulated in at least two of the five evaluated datasets. Pathway enrichment analysis revealed that both of the selected sets are enriched in IFN and acute inflammation response genes (Fig. 1, B and C). As the selected TFs have the highest impact of CRE determination and ranking by LSD, we decided to systematically design SARS-CoV-2 genetic tracing reporters using a combinatorial selection of all TFs and signature gene lists. This resulted in 64 potential reporters (table S1).

To select one of the above-designed reporters that would specifically mark productively infected single cells, we next made use of our recently developed phenotypic ranking approach [Materials and Methods; (*17*)]. First, we aimed at defining genes that would be specific to SARS-CoV-2 infection response by comparative dimension reduction clustering of SARS-CoV and SARS-CoV-2 single cells from parallel single-cell RNA sequencing (scRNA-seq) experiments in one cell type. In Wyler *et al.* (*20*), expression levels of antiviral genes in Calu-3 were twice as high in SARS-CoV-2– compared to SARS-CoV–infected cells at the same time point and in the presence of similar amounts of viral RNAs (*21*). Consistently, we found two cell clusters (C11 and C13) that appear specifically for the response to SARS-CoV-2 based on viral reads accumulation, with C11 having particularly high reads (Fig. 2A). Next, we used our TF binding site (TFBS) enrichment–based phenotypic potential analysis to rank all our reporters (*17*) and found that four sLCRs bear a homogeneous scoring higher than other specific or background reporters when both C11 and C13 were assessed (fig. S1). Our synthetic reporters COVGT1 to COVGT4 markedly outperformed the phenotypic potential of endogenous IFN promoters used in broadly available reporters (e.g., Addgene, #102597, #17596, #30536, and #17598), suggesting that synthetic *cis*-regulatory elements have higher on-target potential than endogenous promoters of the human IFN-γ or IFN-β genes, which are expected to respond to SARS-CoV-2 infection (fig. S1).

To advance reporters that may be representative of primary cell responses in patients, we ranked all the reporters against the nasopharyngeal and bronchial samples from 19 clinically well-characterized SARS-CoV-2 patients with moderate or critical COVID-19 and 5 healthy controls (*7*). The combined signature underlying the design of two distinct sLCRs (COVGT1 and COVGT4) identified two primary cell populations: myeloid cells, notably inflammatory macrophages, and one subpopulation of ciliated epithelial cells with a distinctively strong IFN-γ response signature (Fig. 2B; fig. S2, A and B; and table S1). These SARS-CoV-2 response signature genes were retrieved in three independent cellular models for SARS-CoV-2 infection and are consistent with the pathway analysis of the signature and TF genes (Fig. 1, B and C), suggesting that COVGT1 and COVGT4, cumulatively, could well represent primary host cells in which viral infection triggered an innate immune response. To aim for the highest activity potential, we combined COVGT1 and COVGT4 that combinatorically marked a population of epithelial cells activated by SARS-CoV-2 in patients (Fig. 2C) into one reporter, hereafter referred to as COVGT5 (Fig. 2D).

COVGT5 responds to SARS-CoV-2 and triggers of epithelial innate immunity

To validate the designed reporters, we genetically engineered Calu-3, A549, and 293T cells using transposon- or lentiviral-based vectors. These represent a limited but diverse set of lung cancer and immortalized kidney cell lines. We next tested the individual sLCR expression by fluorescence-activated cell sorting (FACS) and immunofluorescence and found that COVGT5 readily drove the fluorescent protein expression in response to a mix of interferons (IFNs) of all classes (hereon referred to IFN mix; Fig. 3, A and B). This response was more pronounced in immortalized kidney cells compared to lung cancer cell lines. Calu-3 displayed the weakest response to IFNs compared to the other cell lines (Fig. 3A and fig. S3, A to C). All tested sLCRs had low basal expression typically (Fig. 3, A to C; fig. S3, A to C; and Materials and Methods) and were found to be inducible (fig. S3A), which is compatible with screening purposes.

sLCRs may be used to discover external signaling leading to phenotypic state transitions (*15*, *16*). Thus, we next tested specific cues that may potentially drive the response of COVGT5 and be relevant for viral infection biology. COVGT5-modified 293T and A549 cell lines readily responded to individual stimulation by type I IFNs, IFN-α-2a, IFN-α-2b, and IFN-β, as well as synthetic double-stranded RNA transfection but not to IFN-γ, interleukin-28 (IL-28) (IFN-λ), tumor necrosis factor–α (TNF-α), or lipopolysaccharide (LPS) (Fig. 3C and fig. S3D). The marked response to short,

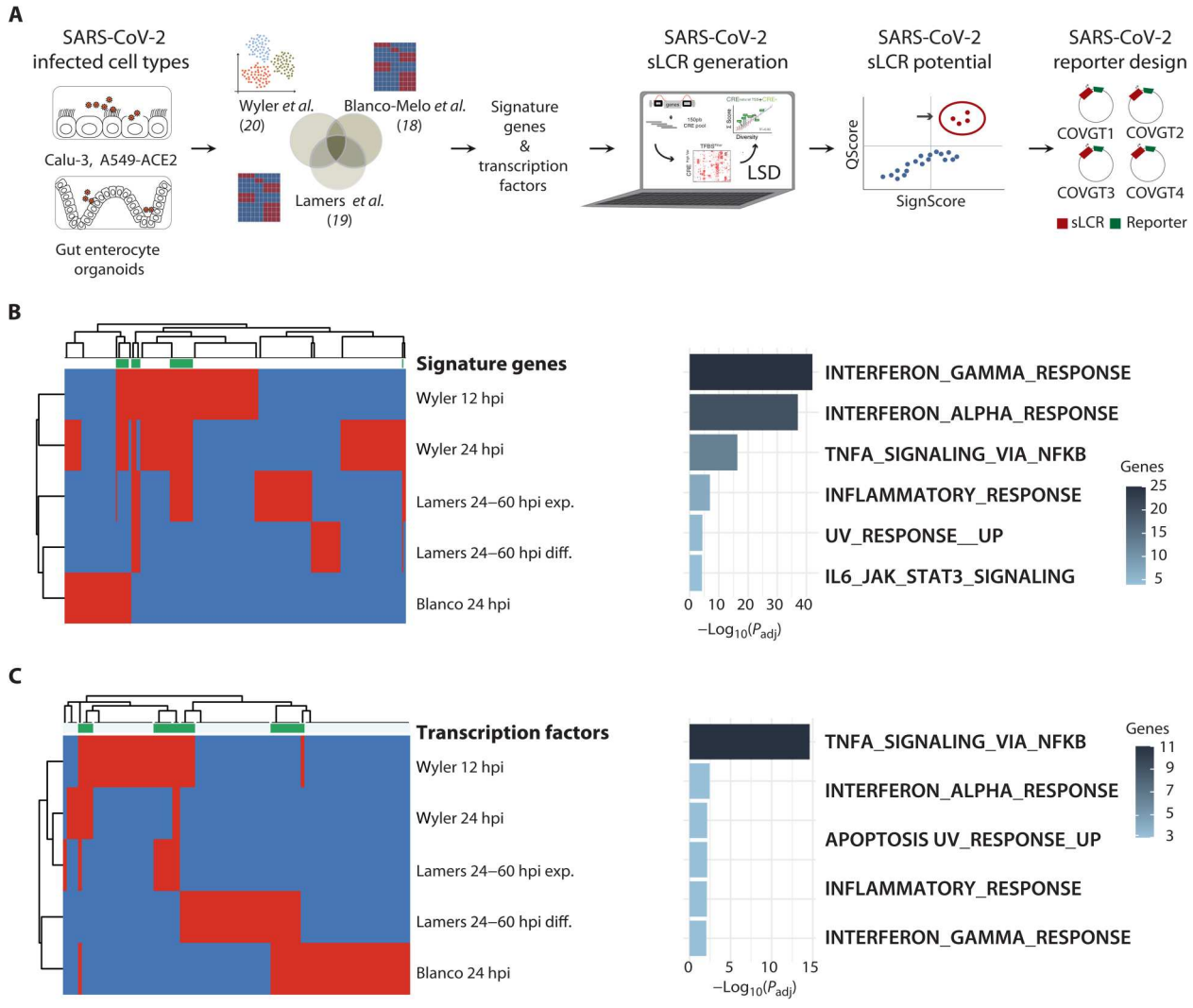

Fig. 1. Generation of COVGT sLCRs from defined inputs using the LSD method. (**A**) Schematic representation of the SARS-CoV-2 sLCR generation. Bulk and single-cell expression profiles from the indicated studies were combined to infer an epithelial response signature to SARS-CoV-2 and define LSD input. (**B** and **C**) Signature selection to generate the SARS-CoV-2 sLCR. Left, heatmaps of ssGSEA enrichment in the indicated dataset for signature genes (B) and TFs (C). Clustering used Euclidean distance, complete linkage. Green denotes the genes meeting the threshold of activation in >2 different common genes among different datasets. Right, molecular hallmarks enrichment analyses.

triphosphorylated stem-loop hairpin RNAs (3p-hpRNAs) as compared to the less specific inducer of PRRs, polyinosinic/polycytidylic acid (pI:C), indicated that RIG-I–mediated innate intracellular double-stranded RNA sensing (*22*) is a key trigger of COVGT5 expression. In agreement with predictions made in silico (Fig. 2C), head-to-head testing experimentally supported that COVGT5 was moderately but significantly more inducible than COVGT1 and COVGT4 in response to both IFN mix and 3p-hpRNA in 293T (fig. S3E) and responds to a wider variety of triggers than IFN-β1 (*23*) and IFN-γ (*24*) promoters cloned within the same backbone, in both 293T and A549 cells (fig. S3F). Hence, we adopted COVGT5 for subsequent experiments.

Next, we tested COVGT5 induction in response to SARS-CoV-2 infection. To this end, we engineered A549-COVGT5 and 293T-COVGT5 lines to overexpress human ACE2, the human receptor for SARS-CoV-2 entry. Extracellular ACE2 enzymatic activity confirmed the successful engineering (fig. S3G) and made both cell lines permissive for infection with all the strains tested (Wuhan, Delta, and Omicron; Fig. 3D). Furthermore, introduction of ACE2 did not affect COVGT5 reporter inducibility in 293T and A549 exposed to the IFN mix (fig. S3H). In a longitudinal live-cell imaging setting using the wild-type Wuhan SARS-CoV-2 strain engineered to express mNeonGreen [icSCV2-mNG (*25*)], A549-ACE2-COVGT5 and 293T-ACE2-COVGT5 lines were permissive to infection and a measurable viral accumulation/replication starting from 72 to 120 hpi (Fig. 3E). COVGT5 response appeared to be proportional to the extent of viral replication in our cell models. A high dose of icSCV2 caused a marked response in 293T-ACE2-COVGT5, which was comparable to IFN stimulation (Fig. 3F). Consistently, in response to low-dose Omicron infection, we observed a moderate but measurable activation of the COVGT5 sLCR, which

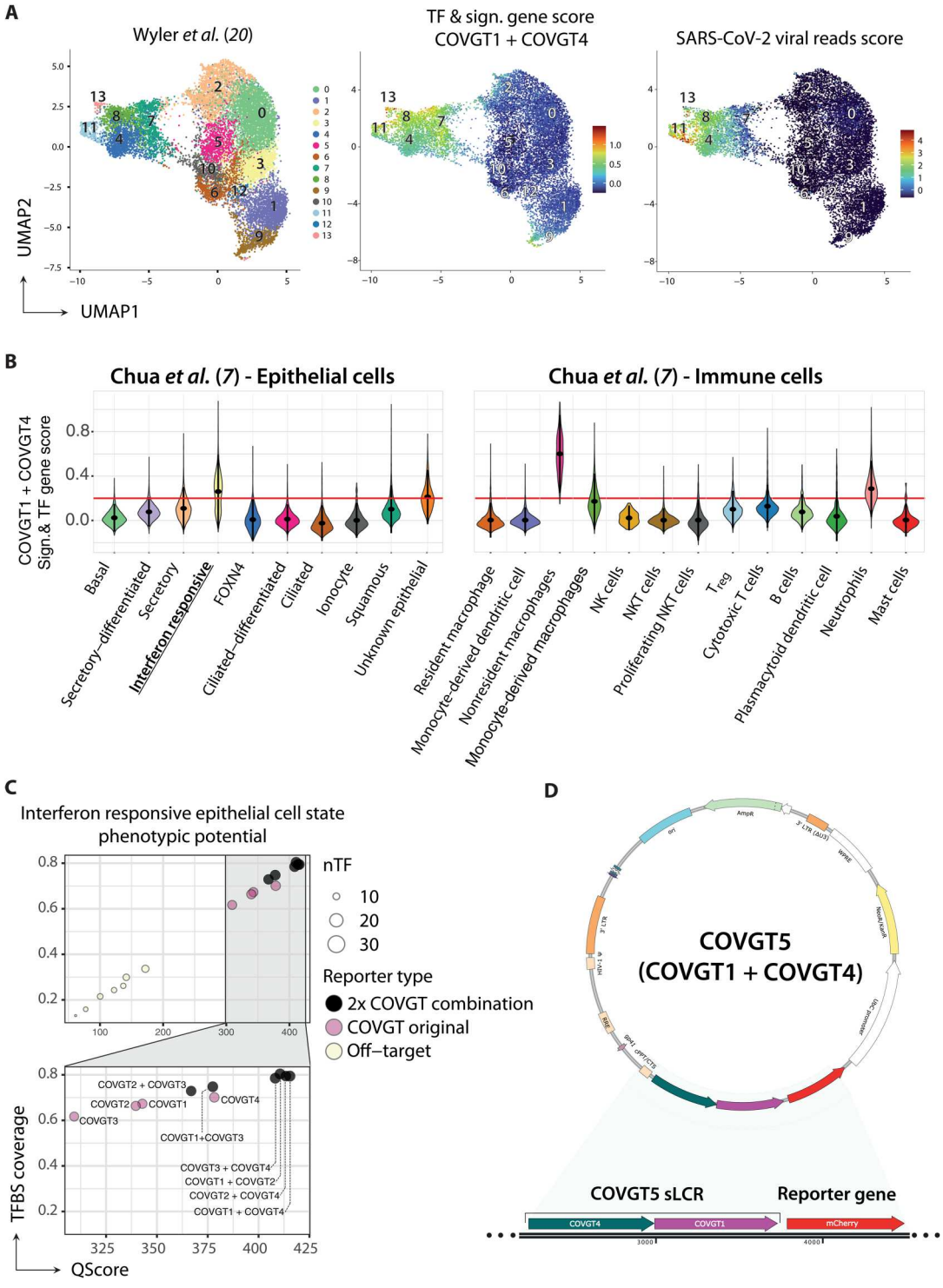

Fig. 2. COVGT5 represents a productive SARS-CoV-2 infection and innate immune response in silico. (**A**) Uniform Manifold Approximation and Projection (UMAP) representation of the Wyler *et al.* (*20*) SARS-CoV/CoV-2 dataset. Colors highlight cell clusters (left), COVGT1 + COVGT4 signature scores (middle), and SARS-CoV-2 viral reads (right). (**B**) Violin plot ranking COVGT1 + COVGT4 against SARS-CoV-2 patient samples. Signature and TF gene scores from COVGT1 + COVGT4 were calculated on annotated cell clusters from Chua *et al.* (*7*). Enrichment scores (*y* axis) of distinct cell clusters (*x* axis) within epithelial (left) and immune (right) cell populations are shown. (**C**) In silico comparison of individual and combined COVGT sLCRs. Six combinations of sLCRs (black) are plotted against individual COVGT sLCRs (pink) and off-target reporters (yellow). Qscore (*x* axis) and TBFS coverage (*y* axis) predict specificity on the target phenotype. The dot size indicates the number of TFs captured from the input list. (**D**) Vector composition of COVGT5-mCherry. Representation of COVGT5 design from a combined COVGT4-COVGT1 sLCR driving mCherry expression.

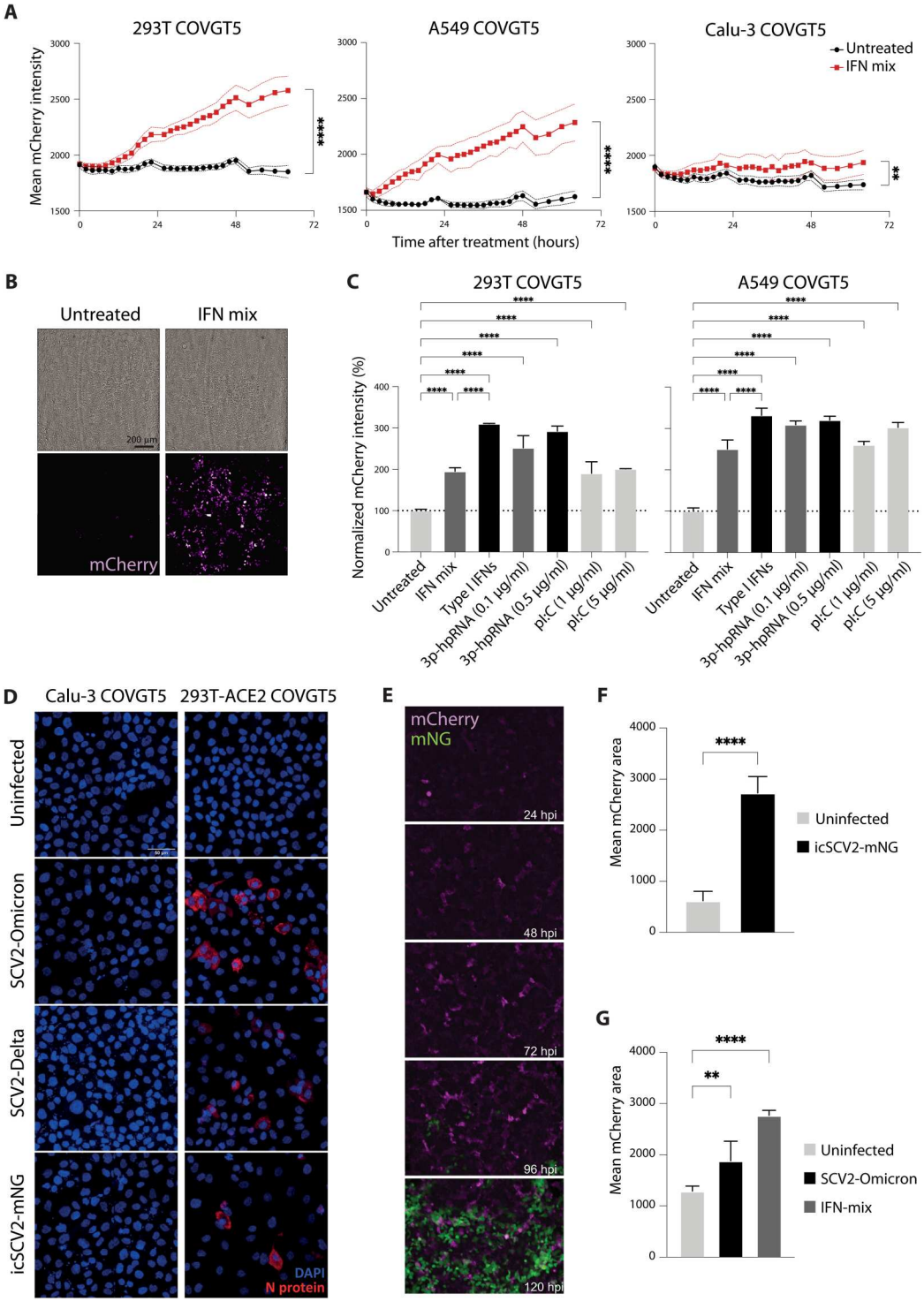

Fig. 3. COVGT5 responds to SARS-CoV-2 and innate immunity activators. (**A**) Longitudinal measurement of 293T, A549, and Calu-3 COVGT5 reporter cells upon IFN mix treatment. Time after treatment is indicated on the *x* axis; each dot represents a single measurement. Mean mCherry intensity was calculated from technical triplicates ($n = 3$) measured by Operetta confocal imaging system, and the confidence interval was plotted. (**B**) Representative images of COVGT5-driven mCherry expression (magenta) in 293T. Images were taken 48 hours after IFN mix treatment. Scale bar, 200 μm. (**C**) Bar plot quantification of COVGT5-driven mCherry up-regulation. COVGT5 induction at 48 hours following IFN mix, 3p-hpRNA (0.1 and 0.5 μg/ml), and pI:C (1 and 5 μg/ml) treatment in 293T and A549 reporter cells was assessed by normalizing against untreated reporter cells. *P* values denote significance by one-way analysis of variance (ANOVA). (**D**) Fluorescence microscopy images of SCV2 infection. N-protein (red) was used as a proxy for productive SCV2 infection with Omicron, Delta, and mNG-engineered Wuhan strain in Calu-3 and 293T-ACE2 reporter cells. Nuclei are counterstained with 4′,6-diamidino-2-phenylindole (DAPI) (blue). (**E**) Longitudinal fluorescence microscopy images of COVGT5-driven mCherry expression (magenta). icSCV2-mNG [6600 plaque-forming units (pfu)/ml] (green) was used to infect 293T-COVGT to visualize productive infection. (**F** and **G**) Bar plot quantification of COVGT5-driven mCherry up-regulation in response to icSCV2-mNG (6600 pfu/ml) (F) and SCV2-Omicron (88 pfu/ml) (G). Measurement by Incucyte was taken at 120 hours post-infection (hpi). The relative mean fluorescent area was determined from technical replicates ($n = 4$). *P* values denote significance by one-way ANOVA.

was delayed and reduced when compared to their response to IFNs (Fig. 3G and fig. S3I).

In our experiments, Calu-3 cells, despite endogenously expressing ACE2 and the TMPSSR2 protease, albeit at low levels, and being initially adopted by the field as a model of choice for in vitro infection biology, proved to be less responsive to IFN signaling (Fig. 3A and fig. S3, B and C). In addition, they appeared to be poorly permissive for infection with all the strains tested, which was confirmed by SARS-CoV-2 N-protein immunofluorescence (Fig. 3D). Overall, our experiments show that COVGT5 responds to type I IFNs, double-stranded RNA, and SARS-CoV-2 viral replication, which are all triggers of epithelial innate immunity.

A platform for discovery of pharmacological modulators of cellular innate immunity and response to SARS-CoV-2 infection

To exploit the specific responses of COVGT5 to triggers of epithelial innate immunity, we next subjected our epithelial cell models to the validated signaling cues and systematically investigated pharmacological modulators of such response. To this end, we assembled a custom library of small molecules against some of the key targets and pathways, including targeted agents approved by the United States Food and Drug Administration (table S2). To screen for modulators of epithelial cell response to COVGT5 activation that may be used in clinics, we used a treatment scheme including three doses in the low-nanomolar to low-micromolar range (i.e., 0.03, 0.3, and 3 μM; Fig. 4, A and B, and fig. S4A). In a 48-hour live imaging setting, we were able to rank selected drugs for their ability to enhance or block COVGT5 activation in response to both IFN mix and 3p-hpRNA and eliminate those drugs that would affect cell viability at low doses/short time points. The top ranked small molecules that blocked COVGT5 activation in both lines and in response to both triggers were well established and clinically relevant JAK inhibitors (JAKis) Baricitinib and Tofacitinib (Fig. 4, B and C, and fig. S4B). The mechanism of action of both drugs is the inhibition of autocrine and paracrine cytokine signaling, with specificity for JAK1-JAK2 (Baricitinib) and JAK3-JAK2 (Tofacitinib), in agreement with the JAK-mediated STAT1 activation caused by type I IFN stimulation of IFNAR. Since COVGT5 activation was efficiently blocked by both JAKis in both cell lines in response to the JAK1-/STAT1–independent trigger 3p-hpRNA, the screen suggests that COVGT5 reports on signaling of both primary and secondary innate immune transcriptional responses in epithelial cells such as the activation of the antiviral and autonomous inflammatory genes.

Among the top amplifiers of COVGT5 activation in response to the aforementioned triggers and across multiple cell lines and doses, we scored several modulators of genome integrity, with the notable case of DNA damage inducers (e.g., TOP1 inhibitor, Topotecan, and TOP2 inhibitor, Etoposide; Fig. 4, B and C, and fig. S4B). The main hits of the screens were separately validated in the reporter cell lines, and specific COVGT5 expression was confirmed (Fig. 4D).

Etoposide and Baricitinib/Tofacitinib antagonistically modulate COVGT5 response to productive SARS-CoV-2 infection

To validate the response observed in the screen using SARS-CoV-2, we next infected 293T-ACE2-COVGT5 with the Omicron strain and simultaneously treated these cells with inhibitors of either TOP2 (Etoposide), JAK (Baricitinib, Tofacitinib and ruxolitinib), or TBK-1/IKK-ε/PDK-1 (BX-795). The latter blocks noncanonical IκB kinase and *IRF-3* activation during innate immune sensing. During the longitudinal monitoring of cell responses, 293T-ACE2-COVGT5 displayed a measurable activation of the COVGT5 sLCR in response to Omicron infection, with a moderate upward trajectory at the predefined end point of 156 hpi. This activation mode appeared to be specific for the viral infection setting since the cellular response to the IFN signaling reached the plateau at 48 hours after cytokine stimulation and lasted until 156 hpi (fig. S4C). In line with the results of our screen, COVGT5 expression was abrogated by all the independent JAKis tested (Ruxolitinib, Baricitinib, and Tofacitinib), as well as by the TBK-1/IKK-ε/PDK-1 inhibitor BX-795 (Fig. 4E). Instead, Etoposide imparted a moderate amplification of the COVIGT#5 signal when administered in parallel to Omicron (Fig. 4E), and a nonlinear regression model supported the hypothesis that Etoposide and JAKi antagonistically modulate COVGT5 response to productive SARS-CoV-2 infection (Fig. 4E). Similar antagonism was observed for the SCV2-mNG strain (Fig. 4F and fig. S4C). Of note, in 293T cells exposed to icSCV2-mNG, similar viral replication levels in individual treatment arms excluded that JAK or topoisomerase inhibitors regulated COVGT5 through viral replication, suggesting that they mainly affect cellular responses through their mechanism of action (fig. S4D). Thus, our data support the use of an sLCR to detect responses to viral infection as a drug discovery platform to identify pharmacological modulators of innate immune responses.

Synergistic and antagonistic pharmacological modulation of COVGT5 underscored drug mechanism of action and convergence on endogenous transcription

The targets of individual JAKis are biochemically well established, and the consequences of signal transduction observed in our experiments aligned with expectations. Cell exposure to chemotherapeutics such as Topotecan and Etoposide leads to far less predictable targets and consequences. We therefore tested whether our reporter could provide evidence supporting the mechanism of action of the drugs controlling its regulation.

DNA damage induces ISGs and the IFN-α and IFN-λ genes via *NF-κB* activation (*13*), which is consistent with both the predicted outcome of TOP1 and TOP2 inhibition by Topotecan and Etoposide, respectively. However, small molecules may also have unrelated, off-target effects. To address whether or not DNA damage is the actual trigger of the SARS-CoV-2 infection–like response observed, we set out to conduct both selective pairwise synergy screens and a comprehensive transcriptomic analysis (Fig. 5A). In 293T-COVGT5 and A549-COVGT5 exposed to IFN mix or 3p-hpRNA, Bliss synergy scoring of the dose escalation for Topotecan and Etoposide determined that the combined treatment synergistically amplified COVGT5 expression, in line with their predicted induction of DNA damage (Fig. 5B and fig. S5A). The extent of synergism was cell line specific and reflected the extent of response to IFN mix (Fig. 5B and fig. S5A). Conversely, JAKi combination synergistically restricted COVGT5 activation (Fig. 5B and fig. S5A), indicating that synergism reveals mechanistical convergence. Thus, we next substituted either Topotecan or Etoposide with ionizing radiation (IR), which is a direct method to damage DNA. IR amplified activation of COVGT5 in dose-dependent manner on top of 3p-hpRNA transfection, and in both lung and kidney cell lines, starting from a dose of 1 Gy (fig. S5B). Bliss synergy scoring of the dose escalation of each combination indicated that IR activation is epistatic to Topotecan or Etoposide (Fig. 5C), supporting that cooperative DNA damage induction occurred. In contrast, Bardoxolone, an *NRF2* activator, antagonistically regulated COVGT5 when combined with Topotecan (fig. S3C), indicating that drugs with distinct mechanisms of action do not synergistically amplify cellular responses to 3p-hpRNA.

Type I IFN responses involve activation of TFs such as IRF3 and IRF7 (*26*) and negative feedback by proteins including SOCS1 and USP18 (*27*). However, in response to viral infection, only a few endogenous genes are strictly dependent on individual factors, as exemplified by experiments in *IRF3* knockout cells (*28*). Consistently,

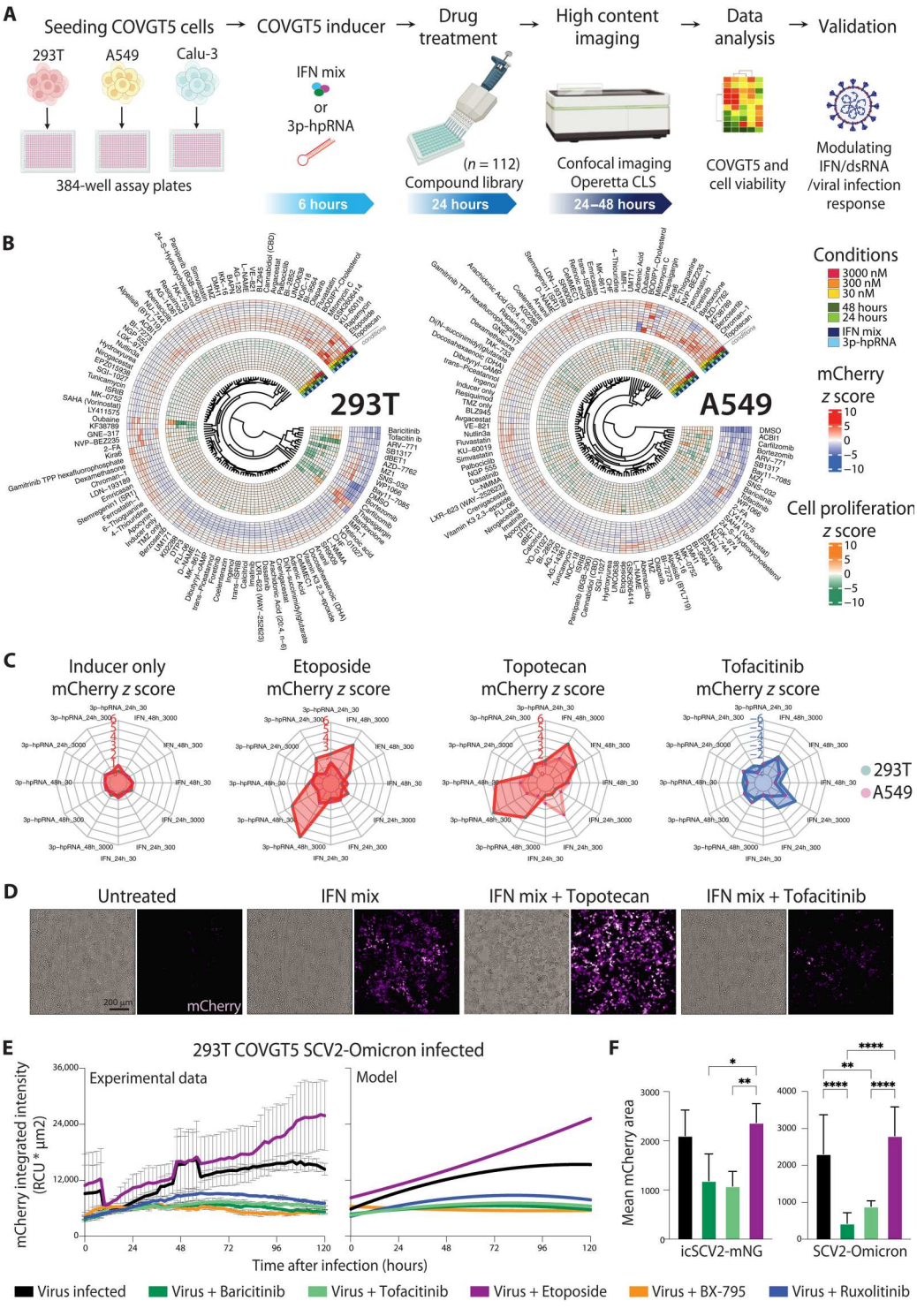

Fig. 4. A platform for discovery of pharmacological modulators of cellular innate immunity and response to SARS-CoV-2 infection. (**A**) Schematic representation of the platform. One hundred twelve pharmacological agents were tested on 293T, A549, and Calu-3 COVGT5 reporter cells using IFN mix and 3p-hpRNA (0.1 μg/ml) as inducers and high-content image acquisition and quantification as readout. (**B**) Circular heatmaps representing screening results of 293T (left) and A549 (right) COVGT5 reporter cells. Drugs were tested in concentrations of 30, 300, and 3000 nM at 24 and 48 hours after induction in technical replicates (n = 4). Z scores calculated for cell viability (inner circle) and mCherry intensity (outer circle) are plotted, and drugs are ordered based on hierarchical clustering for both parameters. (**C**) Spider plots highlighting COVGT5 modulators. Amplifiers (Topotecan and Etoposide) and inhibitors (Tofacitinib) were identified from screening data in 293T (teal) and A549 (purple). Each data point is represented as a corner of the plot with the indicated scale ranges (note for color coding: red, activation; blue, inhibition). (**D**) Representative images showing modulatory drug effect. Topotecan (300 nM) and Tofacitinib (300 nM) were used on top of the IFN mix in 293T reporter cells. Scale bar, 200 μm. (**E**) Longitudinal measurement (left) of COVGT5 modulation in virus infection setting. 293T-COVGT5 were infected with SCV2-Omicron (88 pfu/ml) and treated with 10 μM Baricitinib, 10 μM Tofacitinib, 10 μM Etoposide, 200 nM BX-795, or 2 μM ruxolitinib. Polynomial regression model (right) of longitudinal measurement pronouncing drug effects on COVGT5 induction. Measurement and quantification were performed using Incucyte factoring mean fluorescence intensity and fluorescent area. (**F**) Independent bar plot quantifications of 293T-COVGT5 induction by SCV2 infection. SCV2-Omicron (6600 pfu/ml) or icSCV2-mNG were used with 10 μM Baricitinib, 10 μM Tofacitinib, and 10 μM Etoposide. Measurement and quantification were performed using Incucyte at 120 hpi. The relative mean fluorescent area was determined from technical replicates (n = 4). P values denote significance by one-way ANOVA.

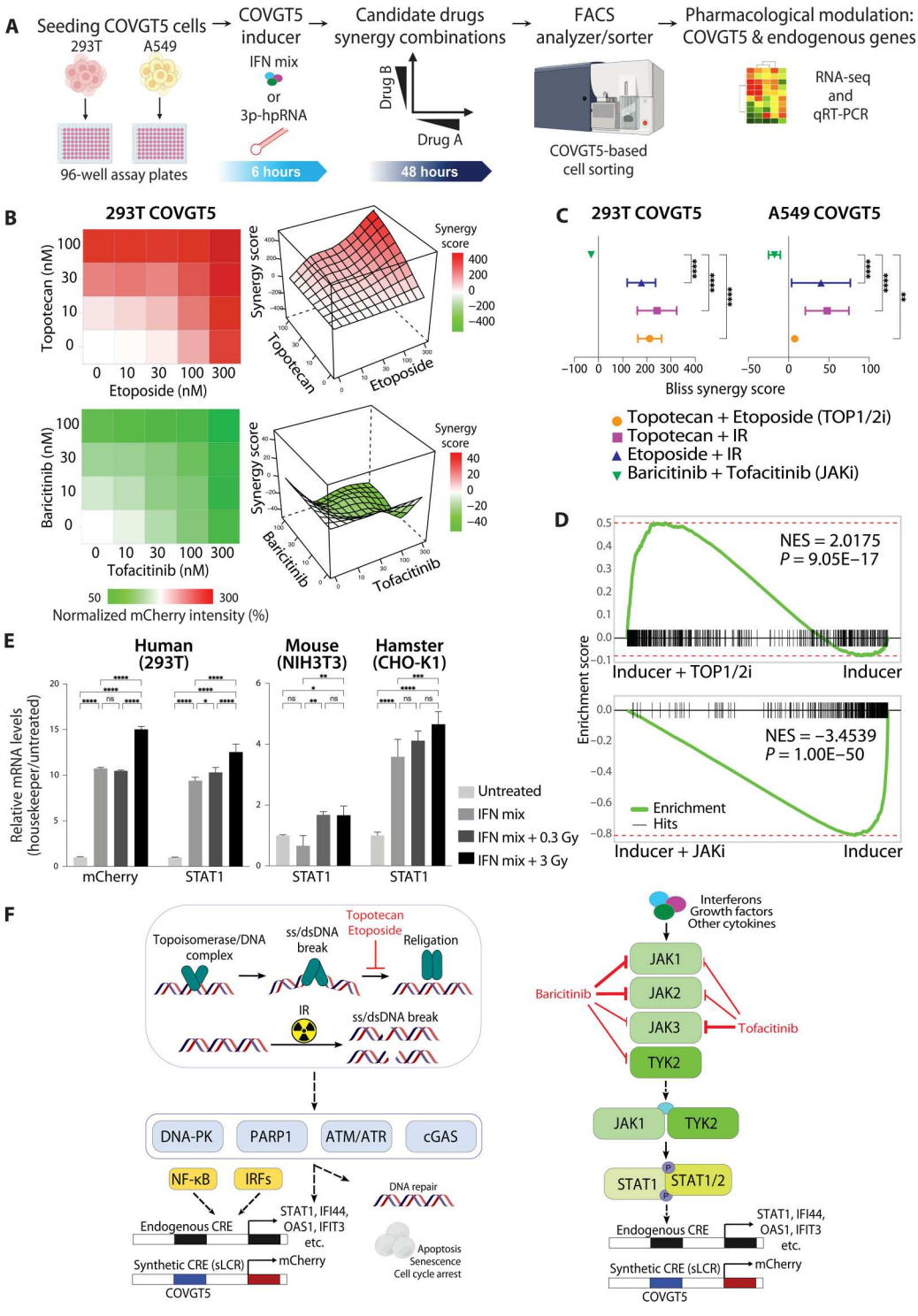

Fig. 5. Synergistic and antagonistic pharmacological modulation of COVGT5 underscored the drug mechanism of action. (**A**) Schematic depiction of approach to define mechanistic basis of COVGT5 regulation. (**B**) Dose escalation of Topotecan against Etoposide (top) and Baricitinib against Tofacitinib (bottom). 293T-COVGT5 received IFN mix induction followed by combinatorial drug treatment. Mean mCherry intensity was calculated from technical triplicates ($n = 3$) and normalized to non–drug-treated cells. Quantification was performed by high-throughput FACS measuring mean mCherry fluorescence intensity. Bliss synergy scores inform on synergism between Topotecan + Etoposide and Baricitinib + Tofacitinib in modulating COVGT5 response. (**C**) Mean Bliss synergy score calculated from all single drug combination data points. Topotecan + IR and Etoposide + IR in addition to drug combinations from (A) in 293T and A549 reporter cells were performed in technical triplicates ($n = 3$). Quantification was performed by high-throughput FACS. *P* values denote significance by one-way ANOVA. (**D**) GSEA plot of IFN mix– and 3p-hpRNA-treated 293T and A549 RNA-seq data ($n = 3$ biological replica) using the COVGT5-coregulated gene signature. COVGT5 inducers are the denominator of the GSEA against the effect of Topotecan + Etoposide amplification (top) or Baricitinib + Tofacitinib (bottom). (**E**) Bar plot showing the expression of the indicated genes in the indicated cell lines by RT-qPCR. Note the conserved response of *Stat1* expression in response to IFN mix and IR in mouse and hamster cells. *P* values denote significance by one-way ANOVA. (**F**) Schematic representation of proposed mechanisms of action for COVGT5 modulation. Pathways for induction and amplification by Topotecan, Etoposide, and IR (left) and COVGT5 inhibition by Baricitinib and Tofacitinib (right) (strength of inhibition arrows indicate specificity) are proposed. ns, not significant.

knockdown of *IRF3*, *IRF7*, and *SOCS1* in 293T and A549 cells did not markedly affect COVGT5 activation in response to IFN mix (fig. S6, A and B), despite *IRF3* and *IRF7* binding sites being included among the input.

To determine whether COVGT5 expression reflects the activation of a broad or cell type– and trigger-specific gene expression program, we next systematically dissected COVGT5-coregulated genes by RNA-seq in FACS-purified cells (Fig. 5A and fig. S6C). Principal components analysis (PCA) indicated that COVGT5 activation and its modulation by antagonistic JAK and TOP1/2 inhibitors dominate gene expression variation together with the expected cell type–specific programs (fig. S6D). We then defined 454 genes coregulated with COVGT5 in a cell type– and trigger-independent manner, and 104 genes were antiregulated (fig. S6, E to G, and table

S3). COVGT5-coregulated genes were generally connected to response to IFNs and viruses, as well as antigen presentation (fig. S6, E and F). The substantial similarity between COVGT5-coregulated genes in cell lines and IFN signatures obtained from primary models (fig. S6F) (*18*) supports the broad validity of our findings. Consistent with functional inference experiments, *IRF3*, *IRF7*, *SOCS1*, or *USP18* was either lowly expressed or not regulated in our models (table S3). COVGT5 signature genes were significantly amplified by low-dose TOP1/2 and depressed by JAKis, respectively (Fig. 5D). Selected genes from the COVGT5 signature such as *IFIT3*, *IFI44*, *OAS1*, and *STAT1* were confirmed by reverse transcription quantitative polymerase chain reaction (RT-qPCR) in A549 and 293T cells (fig. S7). Therefore, unbiased gene expression profiling corroborated our drug screen findings and connected COVGT5 to an endogenous gene expression program.

Stat1 induction by human IFN mix was observed in both mouse NIH3T3 and Chinese hamster ovary (CHO)–K1 cells and amplified by an IR dose of 3 Gy (Fig. 5E), which is on the higher end of the dosage compatible with clinically applicable low-dose radiotherapy (LDRT) (*29*). Hence, *Stat1* conserved induction could be used as an endogenous molecular beacon in preclinical animal models for modulation of type I IFN responses and viral infection.

Together, our data suggest that DNA-damaging agents and JAKi antagonistically modulate epithelial innate immunity in response to SARS-CoV-2 infection (Fig. 5F). These leads were enabled by synthetic genetic tracing for SARS-CoV-2 viral infection in epithelial cells applied in a drug discovery setting and feature its application to infection biology more broadly.

DISCUSSION

COVID-19 pandemic has seen no single drug or combination proven to effectively halt disease progression, and the effect of the massive worldwide vaccination campaign is waning. Additional threats may come from near-future surges of this pandemic by SARS-CoV-2 subvariants, and other pandemic-scale infectious diseases, which are recurrent in history. To grapple with these pressing issues, we report the COVGT sLCRs and the validation of the approach to design such reporters. Together, these form a useful resource for investigating the cellular response to SARS-CoV-2 entry and replication as well as an invaluable tool for high-throughput screening of therapeutics. Combining reporters that measure viral entry and replication with those that measure cellular transcriptional responses is timely (*30*). The flexibility to use such systems in any chosen model, potentially including preclinical models in vivo, is a unique feature of our system. In addition, the adaptability of our system to establish in vitro infection models allows the rapid testing of wild-type and evolving pathogens stains.

Whereas heterogeneous responses to viral infection are likely rooted in biology (*30*), future experiments with this and other reporters will likely benefit from using cellular models that are physiologically more accurate than cell lines. Through our experiments, 293T cells were found to be a more responsive model for triggers of innate immunity and viral infection, while A549 displayed intermediate IFN and RIG-I responses, as well as permissiveness of SARS-CoV-2 infection. On the other hand, we observed limited response in Calu-3, a lung cancer cell line adopted at the start of the pandemic, and later dismissed as an effective model. Hence, synthetic genetic tracing may be used to rapidly screen for the most optimal cellular models for infection biology studies.

The COVGT5 reporter characterized here was independently and strongly activated by type I IFNs and RIG-I agonists in cells and outperformed publicly available reporters both in silico and in vitro, and its expression was connected to endogenous gene expression. RIG-I, a major receptor for viral mRNA sensing, was validated head-to-head in primary cells and cell lines (*31*), supporting the validity of our findings. COVGT5 activation in our epithelial cell models may be modulated by bioactive agents found through in vitro image-based screens. An example is our discovery of DNA damage inducers and JAKis, which act as rheostats of epithelial immunity. Of note, the identification of a cell type– and trigger-independent signature of endogenous innate immune responses suggests that COVGT5 activity may be conserved across various tissues and cell types. On the basis of our past experience with other synthetic reporters (*15*, *16*), identifying and elucidating critical mechanistic nodes of context-specific COVGT5 activation will require phenotypic functional screens at a genome scale or focused on pathways, such as the signature genes we report.

IFN response plays a critical role in the first lines of defense against viral infections. It involves the transcription of IFN genes first and later of ISGs, which in turn lead to an antiviral state in both infected and neighboring cells. Viral infections are detected through PRRs, including RIG-I–like receptors. Notably, SARS-CoV-2 evolution through variants of concern involved increased IFN response evasion (*32*), and a synthetic agonist stimulation of RIG-I protects mice from acute and chronic SARS-CoV-2 infection, even in the absence of the adaptive immune system (*33*). This underscores the importance of epithelial innate immune responses to restrain SARS-CoV-2 infection and supports the potential of pharmacological modulators of such response as a therapeutic strategy to manage COVID-19 and viral infections more broadly. Our COVGT5 sLCR designed on the transcriptional response of lung epithelial and enterocyte organoids to SARS-CoV-2 infection could be explained by activation of IFN- and RIG-I–like signaling. This provides an additional asset for our study as it offers a cellular reporter for viral infection biology and a molecular tool for cellular and molecular dissection of these pathways.

Given the antiviral immunity's pivotal signaling through JAK/STAT pathway, JAKis were already clinically tested as therapeutics for COVID-19. Retrospectively, JAKi appeared potentially helpful to manage disease severity (*3*). Likewise, Topotecan, one of the other drugs uncovered by our COVGT5 reporter as an amplifier of innate immunity, was recently found as treatment to blunt the hyperinflammatory response to anti–SARS-CoV-2 treatment with successful validation in preclinical models (*34*). More generally, topoisomerase 1 and 2 inhibitors are potent modulators of innate immune activation (*35*, *36*). In mice, Topotecan and Etoposide ameliorate responses to colitis (*37*), and Etoposide partly protects from sepsis (*38*), thereby featuring an anti-inflammatory function at systemic level. An ongoing clinical trial is testing Topotecan in COVID-19 patients to assess the safety of a single dose and its potential to blunt inflammation systemically (NCT05083000). Our experiments are focused on epithelial cell–intrinsic responses to triggers of innate immunity and may be helpful to interpret the results of this trial as they suggest that DNA damage modulation may also be effective in priming an antiviral state in vivo or amplifying it. This may occur in both infected and neighboring cells as a

function of cellular state or productiveness of the infection. However, preclinical testing in vivo will be important to investigate the impact of cell type–specific and systemic responses.

Combination therapies were frequently tested in COVID-19 trials, particularly using antiviral drugs as anchor, since those were deemed insufficient if administered at disease progression (*5*). Remdesivir, the first antiviral to show mild effectiveness against COVID-19, appeared to cooperate with Baricitinib (*5*). For JAKis and Dexamethasone, a glucocorticoid receptor agonist that did not consistently modulate our reporter across the screens and validations, trials suggested that drug administration should occur in a particular window of time to promote beneficial effects, or else these drugs could be detrimental (*3*, *4*). In our experiments, all JAKis abrogated cellular response to viral replication, providing support for their use for such purposes. We arrived at our conclusion through a rapid screening of a curated set of drugs. This approach is significantly more scalable than the use of clinical trials and artificial intelligence, which reached a similar conclusion (*39*). Moreover, our platform is uniquely placed to discover drug combinations synergistically acting toward cellular response to viral infection in preclinical models, which may later be tested during disease progression. Alternatively, rather than abrogating epithelial immunity, combinations of drugs that promote an antiviral state and cooperate with antiviral drugs could be tested to potentiate disease control. As supplementing IFN-β-1a in combination with Remdesivir did not improve outcomes and was associated with adverse effects in a placebo-controlled phase 3 trial (*40*), innate immunity amplification will require the identification of safe combinations. Our screen also initially revealed Rapamycin as a potential epithelial immunity amplifier drug. However, this drug was not validated in later experiments. Whether targeted IR may reduce the impact of viral shedding in selected organs is an intriguing hypothesis that stems from this study. Low-dose radiation therapy (LDRT) has been studied as a possible treatment option during the COVID-19 pandemic, yet its effectiveness is still debated (*41*, *42*). Future combinations should focus on approved drugs with higher safety profiles or involve substantial preclinical testing. DNA damage-inducing agents have the potential to worsen cellular responses to an infection (*43*), and heightened IFN responses have been linked to severe COVID-related disorders such as vasculitis, "COVID toes," and Kawasaki-like disease. Nevertheless, our finding that *STAT1* induction by IR within epithelial cells appears to be conserved in mouse and hamster cells, if used at doses slightly stronger than conventional LDRT, offers a possibility of testing LDRT for its potential to be an effective treatment in widely used preclinical models and compare outcomes across species.

The onset of the COVID-19 pandemic resulted in substantial global morbidity and mortality, and led to worldwide economic collapse due to the lack of early preparedness. Our approach took 4 weeks from the discovery of the first transcriptional signatures to validate the reporter and offers significant potential for optimization, thus making synthetic genetic tracing more available for infection biology in the future.

MATERIALS AND METHODS

Datasets

The data to generate the signature genes and TFs listed in Fig. 1 were downloaded from Gene Expression Omnibus, accession GSE148729 and GSE147507, or the Supplementary Materials (see below).

LSD reporter design

COVGT reporters were designed using the LSD method, as described (*17*). Briefly, the LSD algorithm takes a list of PWMs, a list of marker genes of a target phenotype, and the reference genome of the organism of interest, and it generates a list of naturally occurring, putative *cis*-regulatory elements used to assemble the synthetic reporter. The algorithm can be divided into three steps. In step I, LSD generates a pool of potential CRE with a fixed length within user-defined regulatory landscapes [default is a 150–base pair (bp) window sliding with a 50-bp step]. In step II, LSD assigns TFBSs to the CRE pool using FIMO (default --output-pthresh 1e-4 --no-qvalue) and creates a matrix of putative CREs × TFBS. In step III, LSD ranks and selects the minimal number of CREs representing the complete set of TFBS. For that purpose, it uses an algorithm to sort and select the best CRE based on the overall TFBS affinity and diversity among input TFs showing high affinity for the CRE. Starting from the ranked CREs, LSD selects the highest-ranking CRE defined by the sum of the affinity score [$-\log_{10}(P \text{ value})$] and TFBS diversity (number of different TFBS). Subsequently, it removes the selected CRE and the corresponding TFBS from the CRE × TFBS matrix and repeats the selection. This continues until either none of the CRE or of the TFBS is left. In the ranking, priority is given to CREs proximal to known transcription start site (TSS) based on 5′ CAGE data (ENCODE) to increase the chances of successful transcriptional firing using the same strategy as above. Last, LSD returns an ordered list of the selected CREs, together with a representation of the TFBS scores (Fig. 1A). LSD is available at: https://gitlab.com/gargiulo_lab/sLCR_selection_framework. All COVGT sLCRs are available from Addgene either with destabilized GFP or additionally with mCherry as fluorophores (https://www.addgene.org/Gaetano_Gargiulo/; Addgene IDs #201447, #201448, #201446, #201449, #201451, #201452, #201450, #201453, #201454, #201455). The COVGT5 plasmid #201454 pPB-Neo-COVGT5-d2EGFP-mCherry was primarily used in this study.

Cis-regulatory potential assessment of the SARS-CoV-2 sLCRs

To generate a common SARS-CoV-2 signature and define the specific TF (Fig. 1A), we integrated different transcriptional profiles available at the moment of this publication. We first downloaded Blanco-Melo *et al.* (*18*) (GSE147507), Wyler *et al.* (*20*) (GSE148729; www.mdc-berlin.de/singlecell-SARSCoV2), and Lamers *et al.* (*19*) (differentially expressed tablets). Then, we reanalyzed Blanco-Melo *et al.* (*18*) and Wyler *et al.* (*20*) using the same parameters as in the publications. Blanco-Melo *et al.* (*18*) and Lamers *et al.* (*19*) gene signatures and TF were selected using $\log_2 FC > 1$ and adjusted *P* value (P_{adj}) < 0.05. Wyler *et al.* (*20*) gene signatures were identified by using the FindMarkers function (Seurat v.3.1, R v.3.6) and selected using $P_{adj} < 0.05$ as a threshold. scRNA-seq TF selection was generated by selecting exclusive highly

expressed (quantile >75%) TF genes. Integration of the datasets to construct the common gene signatures was done using at least three common genes between experiments, and two common TF genes to define the TF input. Further analysis of TF using Ingenuity Pathway Analysis (IPA) generated the final set of TFs and TFBS used in the different comparisons (fig. S1 and table S1). Previously published reporters carrying promoters of the human IFN-γ or IFN-β genes were included as benchmark (Addgene, #102597, #17596, #30536, and #17598). SARS-CoV-2 sLCR pool was designed using a combination of individual and common datasets and the LSD framework. The inference of the specific phenotypic potential () of each reporter was defined as the linear correlation between the Qscore (affinity-score) and the SignScore (phenotypic-score). The affinity-score (QScore) was calculated for each reporter as the sum of the TFBS-affinity using FIMO (default --output-pthresh 1e-4 --no-qvalue) given a specific set of TFBS (e.g., using as reference IPA selected COVGT#1 TFBS) and normalized by the sLCR sequence length and the ratio of observed/expected TFBS [Σ (FIMO-score) × sequences length)/(observed/expected TFBS)]. In contrast, the phenotypic score (SignScore) was defined as the ssGSEA-enrichment value calculated on target expression profiles (ssgsea.norm=FALSE) using the signature genes, and normalized by the ratio of observed/expected TFBS [ssGSEA-score × (ratio observed/expected TFBS)]. Heatmaps and gene set enrichment analysis (GSEA) (Fig. 1, B and C) were generated using common genes and selection with pheatmap v.1.0.12 and piano v.2.0.2, respectively. Hg19 assembly was used to extract references and generate the sLCR vectors. Scatter plot graphics were generated using ggplot2 on an R v.3.6 environment.

Signature scoring on scRNA-seq datasets

Two scRNA-seq studies were used to establish scores for the COVGT5 signature list consisting of marker genes and TFs. From Wyler *et al.* (*20*), we downloaded the Seurat object file and retrieved annotations for viral reads (SCoV1-ORF1a, SCoV1-ORF1ab, SCoV1-S, SCoV1-ORF3a, SCoV1-ORF3b, SCoV1-E, SCoV1-M, SCoV1-ORF6, SCoV1-ORF7a, SCoV1-ORF7b, SCoV1-ORF8a, SCoV1-ORF8b, SCoV1-N, SCoV1-ORF10, SCoV1-UTR3, SCoV2-orf1ab, SCoV2-ORF10, SCoV2-ORF3a, SCoV2-E, SCoV2-M, SCoV2-ORF7a, SCoV2-ORF8, SCoV2-N, and SCoV2-3′UTR: accession numbers: AY310120 for SARS-CoV and MN908947 for SARS-CoV-2). The list of viral reads as well as the list of signature genes and TFs for COVGT5 generation were used to calculate the meta-module score on single cells using the AddModuleScore() function from Seurat. Similarly, from Chua *et al.* (*7*) and https://digital.bihealth.org, we downloaded the Seurat object and used the AddModuleScore() function to determine enrichment of the COVGT5 signature list over the annotated cell clusters.

Cell lines

All lines used in this study were thawed from frozen batches and propagated for a limited number of passages (10× to 15×), and all lines regularly tested with the Mycoplasma Detection Kit (Jena Bioscience, 11828383, PP-401 L) to exclude contamination. 293T and A549 cell lines [R. Bernards laboratory, Netherlands Cancer Institute (NKI), Amsterdam, the Netherlands] were cultured in Dulbecco′s modified Eagle′s medium (DMEM) or RPMI 1640 medium (Gibco), respectively, supplemented with 10% fetal bovine serum (FBS; Gibco) and penicillin-streptomycin (100 U/ml; Gibco) at 37°C in a 5% CO_2 and 95% air. Calu-3 [L.Č.-Š. laboratory, Helmholtz Centre for Infection Research (HZI), Braunschweig, Germany] were cultured in DMEM (Gibco), supplemented with 1× MEM nonessential amino acid mix (Gibco), 1× sodium pyruvate (Gibco), 10% FBS (Gibco), and penicillin -streptomycin (100 U/ml; Gibco) at 37°C in a 5% CO_2 and 95% air.

Murine NIH3T3 cells were cultured in DMEM supplemented with 10% FBS (Gibco) and penicillin-streptomycin (100 U/ml; Gibco) at 37°C in a 5% CO_2 and 95% air. The hamster ovary–derived cell line CHO-K1 was cultured in DMEM-F12 supplemented with 10% FBS (Gibco) and penicillin-streptomycin (100 U/ml; Gibco) at 37°C in a 5% CO_2 and 95% air.

Transfection/transduction

Transfection and transduction were previously described in detail (*11*). Briefly, 12 μg of DNA mix (lentivector, pCMV-G, pRSV-REV, pMDLG/pRRE) was incubated with the FuGENE (Promega, E2311)–DMEM/F12 (Life Technologies, 31331) mix for 15 min at room temperature, added to the antibiotic-free medium covering the 293T cells, and the first tap of viral supernatant was collected at 40 hours after transfection. Titer was assessed using the Lenti-X p24 Rapid Titer Kit (Takara, 631280) according to the manufacturer′s instructions. We applied viral particles to target cells in the appropriate complete medium supplemented with protamine sulfate (2.5 μg/ml). After 12 to 14 hours of incubation with the viral supernatant, the medium was refreshed with the appropriate complete medium.

COVGT reporter cell lines

COVGT1 to COVGT4 reporter cell lines were generated by PiggyBac vector delivery: 3 μg of Super PiggyBac Transposase (System Biosciences, PB210PA-1-SBI) and 3 μg of reporter plasmid (pPB-{COVGT1}>d2EGFP, pPB[-{COVGT2}>d2EGFP, pPB-{COVGT3}>d2EGFP, pPB-{COVGT4}>d2EGFP) were transfected. Transfected cells were selected using G418 (1 mg/ml; Sigma-Aldrich). COVGT5 reporter cell lines were generated through lentiviral transduction with pBA407-{COVGT5}>mCherry. The backbone of pBA407 was a gift from J. Weissman (Addgene, #85970; RRID:Addgene_85970). Infected cells were selected using G418 (1 mg/ml; Sigma-Aldrich). ACE2 expression 293T and A549 reporter cell lines were generated through lentiviral transduction with pscALPSpuro-HsACE2 (human) (Addgene, #158081). Infected cells were selected using puromycin (2 μg/ml; Sigma-Aldrich). IFN-Beta_pGL3 was a gift from N. Manel (Addgene, #102597; RRID:Addgene_102597) and human -204 IFN-γ luc was a gift from H. Young (Addgene, #17596; RRID:Addgene_17596). Both promoters were amplified by PCR and cloned in pBA407 using HiFi mastermix (NEB).

FACS analysis and sorting

Transduced cell lines were harvested into single-cell suspensions, resuspended into cold medium, and filtered through 40-μm mesh filters (BD) into FACS tubes. Sorting was conducted using BD FACSAria III or Fusion; analysis was conducted on BD LSR Fortessa. The appropriate laser-filter combinations were chosen depending on the fluorophores being sorted for [green fluorescent protein (GFP) or mCherry]. Typically, to remove dead cells, events were first gated on the basis of shape and granularity [forward scatter (FSC)–A versus sideward scatter (SSC)–A] and doublets were

excluded (FSC-A versus FSC-H). If insufficient, alternative gates were used (FSC-W and SSC-W). Positive gates were established on parental cells; untreated reporter cells and IFN mix induced reporter cells to sort for populations with fluorescent signal above background (fig. S3, A, B, and H). For identification of COVGT5-coregulated genes by RNA-seq, 293T and A549 COVGT5 reporter cells were treated with IFN mix or 3p-hpRNA (0.1 μg/ml, inducer). Drug combinations of 30 nM Topotecan + 100 nM Etoposide (TOPi) or 100 nM Baricitinib + 300 nM Tofacitinib (JAKi) were added 6 hours later. The following sorting strategy was applied 48 hours later based on mCherry intensity (fig. S6C): untreated—between bottom 25% and top 75% mCherry intensity; inducer—above top 20 or 30% mCherry intensity; inducer + TOPi—above top 30% mCherry intensity; inducer + JAKi—below bottom 40% mCherry intensity. A total of 2×10^5 to 1×10^6 cells per sample were sorted. Three samples were sorted for each treatment condition and cell line.

COVGT reporter induction

For COVGT reporter induction, cells were seeded at a density of 2000 in 50 μl (for 384-well plates, Greiner) or 10,000 in 100 μl (96-well plates, Greiner) of cells per well and incubated at 37°C in a 5% CO_2 and 95% air for 1 to 2 days until a confluency of 60 to 80% was reached.

Cells were treated with individual cytokines (PeproTech) or COVGT induction mixes: inflammation medium—TNF-α (5 ng/ml), IFN-γ (10 ng/ml), IL-4 (10 ng/ml), epidermal growth factor (EGF) (10 ng/ml), and IL-6 (10 ng/ml); IFN mix—IFN-α-2a (20 ng/ml), IFN-α-2b (20 ng/ml), IFN-β-2b (20 ng/ml), IL-28 (IFN-λ, 10 ng/ml), and IFN-γ (5 ng/ml); 3p-hpRNA, pI:C (InvivoGen), and LPS (Sigma-Aldrich)—transfected at indicated concentrations following transfection protocol described above. Quantification of reporter expression was performed by FACS or Operetta CLS typically 48 hours following induction. For direct comparison of COVGT5 with COVGT1, COVGT4, IFN-β1, and IFN-γ promoter reporters, cells were treated with IFN mix, IFN-β (20 ng/ml), IFN-γ (20 ng/ml), or 3p-hpRNA (1 μg/ml).

Knockdown using siRNA

To knock down IFN response–regulating genes, small interfering RNAs (siRNAs) were transfected into 293T and A549 cells harboring the COVGT5 reporter (siRNA-IRF3, SignalSilence, #6274; siRNA-IRF7, SignalSilence, #13139; esiRNA-SOCS1, Sigma-Aldrich, EHU903081; nontargeting siRNA). Per nucleofection, 30 pmol of each siRNA was prepared in SF buffer (Lonza) and nucleofected into 293T and A549 cells using the AMAXA 4D Nucleofector (Lonza). After 72 hours, a second nucleofection with the same conditions was performed before cells were seeded on 12-well plates with or without IFN mix treatment, and the remaining cells were pelleted and lysed for Western blot evaluation of knockdown efficiency. FACS-based reporter readout was done at 48 hours after stimulation.

Western blot

Radioimmunoprecipitation assay (RIPA) buffer [20 mM tris-HCl (pH7.5), 150 mM NaCl, 1 mM EDTA, 1 mM EGTA, and 1% NP-40] was used to lyse cell pellets. RIPA was supplemented with 1× protease inhibitor cocktail (Roche), 10 mM NaPPi, 10 mM NaF, and 1 mM sodium orthovanadate. Bio-Rad protein assay dye was used for protein determination. The lysates were sonicated if necessary, and protein electrophoresis was performed with NuPAGE Novex 4 to 12% bis-tris precasted gels in NuPAGE Mops SDS running buffer (50 mM Mops, 50 mM tris base, 0.1% SDS, and 1 mM EDTA; Life Technologies). Proteins were transferred onto nitrocellulose membranes (0.2 μm; Amersham-Protran) in transfer buffer [25 mM tris-HCl (pH 7.5), 192 mM glycine, and 20% methanol]. The membranes were blocked at room temperature for 1 hour with 5% bovine serum albumin (BSA) in phosphate-buffered saline (PBS). The primary antibodies were diluted in PBS plus 5% BSA, and membranes were incubated overnight at 4°C. The appropriate horseradish peroxidase–coupled secondary antibodies were used for detection. Bands were visualized using an enhanced chemiluminescence detection reagent (GE Healthcare). Primary antibodies used against the following antigens were as follows: anti-vinculin (mouse clone h-VIN1; Sigma-Aldrich, #V9131), anti-IRF3 [(D6I4C) XP] rabbit monoclonal antibody (mAb) (#11904), anti-IRF7 (D2A1J) rabbit mAb (#13014), and anti-SOCS1 (A156) antibody (#3950).

Fluorescence microscopy

Operetta CLS (PerkinElmer) and Incucyte (Sartorius) were used to acquire fluorescence imaging data of COVGT5 induction. Reporter cell lines were plated on black 384-well or 96-well plates for optical imaging (Greiner) for Operetta CLS high-content confocal imaging. We used the nonconfocal mode and a 10× air objective to image the well center in live-cell imaging mode with temperature and CO_2 control at 37°C in a 5% CO_2. Optimal z position was determined by performing z-stack analysis on control wells before whole-plate acquisition. Light-emitting diode power and detector exposure time were adjusted on induced and noninduced control wells. Images were generally taken at 24 and 48 hours after induction or in a longitudinal setting over 72 hours with image acquisition every 2 to 4 hours. Longitudinal image acquisition and SARS-CoV-2–infected experiments were performed on 96-well plates for optical imaging (Greiner) using the Incucyte live-cell analysis system with temperature and CO_2 control at 37°C in a 5% CO_2. Infected cells were generally imaged every 2 hours after initial infection up to 5 to 8 days.

Image quantification

Following acquisition, quantification was performed using the Harmony software (PerkinElmer) for Operetta CLS images: After filtering each channel (sliding parabola 10px), we used the Harmony software building blocks to identify fluorescent objects above background mCherry intensities. Fluorescent objects were filtered by applying a threshold for object size, and mean intensities as well as number of objects were determined. As a proxy for cell viability and fitness, cell density area was calculated from filtered brightfield images. Data with all relevant parameters were exported as csv files and analyzed using RStudio and GraphPad Prism. Mean fluorescence and viability score were calculated from technical replicates (n = 3 or 4) and normalized to COVGT5-induced but non–drug-treated control wells.

Quantification of Incucyte images was performed using the Incucyte analysis software (Sartorius): Incucyte software identifies whole-cell layer area and fluorescent area above background within the image area and calculates mean fluorescence intensity. Data with all relevant parameters were exported as csv files and analyzed using GraphPad Prism. Mean fluorescent area was calculated

in relation to cell layer area to account for cell toxicity. Integrated mCherry intensity was calculated by factoring mean fluorescent area with mean fluorescence intensity to gain a total fluorescence score. Incucyte experiments were performed with technical replicates ($n = 4$). Statistical testing was done through one-way analysis of variance (ANOVA) with multiple comparisons testing. The trend lines in Fig. 4E are based on second-order polynomial regression fitting implemented through GraphPad Prism v9.4 using the "Interpolation" function.

ACE2 enzyme activity assay

ACE2 enzymatic activity was assessed using an mMCA peptide–based substrate assay (a gift of M. Lebedin and K. de la Rosa, Max Delbrück Center, Berlin, Germany) releasing a fluorophore upon cleavage by ACE2. For this, ACE2-expressing 293T and A549 reporter cells were seeded at 20,000 cells per well on a 96-well plate for optical imaging (Greiner) and incubated overnight at 37°C and 5% CO_2. Mca-APK(Dnp) substrate (Enzo Life Sciences) was diluted 1:100 in Epelman buffer [75 mM tris-HCl (pH 6.5) and 1 M NaCl] supplemented with protease inhibitor mix and 100 μM $ZnCl_2$. Medium was removed before substrate addition. Twenty microliters of diluted MCA substrate was added per well, and fluorescence (excitation, 340 nm; emission, 420 nm) was measured every 30 min following substrate addition using Tecan Spark (Tecan) with temperature control at 37°C. Activity was referenced to recombinant ACE2 protein and parental 293T and A549 reporter cells. Statistical testing was done through one-way ANOVA with multiple comparisons testing.

SARS-CoV-2 viral infection

All SARS-CoV-2 variants and associated experiments were handled in the biosafety level 3 laboratory (L.Č.-Š.'s laboratory, HZI, Braunschweig, Germany). For 293T-ACE2-COVGT5 infection experiments, 20,000 cells per well were seeded in 100 μl of medium and incubated overnight at 37°C and 5% CO_2. Cells were infected with SARS-CoV-2 variants and subsequently treated with drug modulators at indicated concentrations. Longitudinal measurement of COVGT5 induction was performed as described above.

Drug screening

High-content drug screening for COVGT5 induction modulators was performed using the Operetta CLS (PerkinElmer). For this, 293T, A549, and Calu-3 COVGT5 reporter cells were seeded at 2000 cells per well (293T and A549) or 10,000 cells per well (Calu-3) depending on cell growth rate in 50 μl of respective medium. Cells were kept at 37°C and 5% CO_2 for 2 days until a confluency of 60 to 80% was reached. Reporter cells were treated with IFN mix or 3p-hpRNA (only 293T and A549) following the above-described procedure and incubated at 37°C and 5% CO_2. Five to 6 hours after initial induction, cells were treated with drug library. For this, drugs were prepared in a serial dilution setting using respective cell medium to reach final concentration of 30, 300, and 3 μM in technical replicates ($n = 4$) and final dimethyl sulfoxide concentration < 0.5%. Confocal fluorescence images were acquired 24 and 48 hours after initial induction following the above-described procedure. Image quantification was performed as described above. Data containing quantified parameters on COVGT5 fluorescence intensities and cell area were imported as csv files and analyzed using R (v.4.1.2) and RStudio. After data merging and cleaning, drug concentrations were matched to COVGT5 intensities and cell area counts. For each cell line, time point, and concentration, z scores for COVGT5 mean intensity and mean cell area were calculated separately and merged back into a combined data frame. Hexagonal plots, bubble plots, spider plots, and lollypop plots with COVGT5 and cell area z scores were plotted using the ggplot2 (v.3.3.6) package. To generate circular heatmaps, the circlize package (v.0.4.15) was used.

FACS analysis of reporter modulation

All analyses were performed using FlowJo_v10. For quantification of mean fluorescence intensity, mCherry-positive gates were established following doublet exclusion. Mean fluorescence values of technical triplicates ($n = 3$) for each treatment condition were calculated and normalized to IFN mix– or 3p-hpRNA–induced but non–drug-treated condition. Data were exported as csv files and further analyzed using RStudio and GraphPad Prism.

Bliss drug synergy experiments

Drug and pathway synergy experiments were performed in 293T and A549 reporter cells using high-throughput FACS readout. For this, cells were seeded on 96-well cell culture plates (Sarstedt) at 10,000 cells per well in 100 μl of respective medium. Cells were kept at 37°C and 5% CO_2 for 2 to 3 days until a confluency of 60 to 80% was reached. First, cells were treated with IFN mix or 3p-hpRNA as described above and incubated at 37°C and 5% CO_2 for 5 to 6 hours. Drug combinations were dispensed using the D300e digital dispenser (Tecan) in technical triplicates ($n = 3$). For ionizing irradiation, cell plates were treated using the XenX irradiator (Xstrahl) under nonfocused, open beam setting. Cells were incubated at 37°C and 5% CO_2 for 2 days. FACS measurement and quantification was performed as described above. Data were exported as csv files and analyzed using GraphPad Prism to generate heatmaps and RStudio to calculate Bliss synergy using the synergyfinder (v.3.15) package. Mean synergy score was calculated by averaging across all combination data points. Statistical testing was done through one-way ANOVA with multiple comparisons testing.

RNA-seq generation

RNA was extracted using the TRIzol reagent (Invitrogen), with subsequent isopropanol precipitation and AMPure XP bead purification. The concentration of the RNA was assessed by NanoDrop and the Qubit RNA HS Assay Kit (Invitrogen). The integrity of the RNA was determined by means of the High-Sensitivity RNA ScreenTape System (Agilent).

Total RNA was extracted using the TRIzol reagent (Invitrogen) with subsequent isopropanol precipitation, deoxyribonuclease I treatment, and purification with AMPure XP beads (Beckman Coulter). The concentration of the RNA was quantified by the Qubit RNA HS Assay Kit (Invitrogen). The integrity of the RNA was determined with the High-Sensitivity RNA ScreenTape System (Agilent). Sixty nanograms of total RNA per sample was used as input for constructing multiplexed 3′-cDNA (complementary DNA) libraries using barcoded oligo-dT primers (*44*) in an adapted version of bulk RNA barcoding and sequencing protocol (*45*). The final multiplexed library pools were quantified with the Qubit dsDNA HS Assay Kit (Invitrogen) and the Collibri Library Quantification Kit (Invitrogen), and the proper library fragment distribution was assessed by the TapeStation High-Sensitivity

D1000 ScreenTapes Kit (Agilent). Sequencing of the pooled libraries was performed on NovaSeq 6000 in a paired-end mode (read 1, 28 bp; index i7, 10 bp; index i5, 10 bp; read 2: 90 bp). The initial demultiplexing based on Illumina indices was performed using the bcl2fastq conversion software (v2.20.0). Next, the oligo-dT barcode sequences were extracted from read 1 reads using cutadapt (v2.1) and used for subsequent internal demultiplexing using BRBseqTools-1.6.jar (http://github.com/DeplanckeLab/BRBseqTools). The demultiplexed data were aligned to a custom genome (COVGT5 containing GRCh38) using STAR (v2.7.8a), and the count matrices were subsequently generated using HTSeq (v2.0.2).

RNA-seq analysis

R v4.1.2 was used to conduct RNA-seq analysis for COVGT5-induced and FAC-sorted samples. Following gene alignment and counting, DESeq2 (v.1.36) was used to process raw counts and perform differential expression analysis between COVGT5-induced plus or minus TOPi/JAKi and untreated samples. Count matrices from both independent RNA extractions and library preparations for 293T and A549 cells were merged and combined into DESeqDataSetObject with the design formula ~ cell_line + comparison accounting for regression of the cell line–specific batch effect. After filtering for low count genes (rowSums < 1) and lncRNA, variance stabilizing transformation was applied. PCA was used to visualize sample clustering after applying the limma (v.3.50) removeBatchEffect() function. Following the standard DESeq2 workflow, after modeling raw counts, differential gene expression was calculated for each comparison. If genes displayed $\log_2$FC > 1 and P_{adj} < 0.05, they were called as differentially regulated. For further processing and visualization, ENSEMBL-IDs were mapped to gene symbols using the EnsDb.Hsapiens.v75 database. The COVGT5-coregulated gene set was derived from the list of up-regulated genes of the comparison between IFN mix + 3p-hpRNA–treated (inducer) against untreated control cells from both cell lines ($\log_2$FC > 1.5 and P_{adj} < 0.05). The graphics for displaying RNA-seq results were created using ggplot2 v3.4.1 (PCA plot) and pheatmap v1.0.12 (heatmap with hierarchical similarity measure based on Pearson correlation and the "average" clustering method).

Gene set enrichment analysis

GSEA was performed to determine enrichment of biological pathways and the manually curated gene sets (including the COVGT5-coregulated gene set) in the selected comparisons with differentially expressed genes from RNA-seq profiles of FAC-sorted cells. GSEA was performed using the fast-pre-ranked GSEA (fgsea) R package v.1.20, with all genes included in the comparison. The genes were preranked using the Wald statistic obtained from differential expression analysis ($\log_2$FC divided by its SE) for the relevant comparisons. Enrichment scores, normalized enrichment scores (NESs), and P_{adj} (Benjamini-Hoechberg correction) on gene sets of the Gene Ontology Biological Process (GOBP) collection in MSigDB (c5.go.bp.v7.4.symbols) as well as manually curated gene sets were calculated with the default settings for the fgseaMultilevel() function. For visualization, independent pathways were collapsed from the total list using the collapsePathways() function and filtered for the top 10 and bottom 10 NES entries and plotted as an enrichment tablet. Enrichment statistics from manually curated gene sets were either plotted using the plotEnrichment() function or extracted into a data matrix and visualized using pheatmap (v.1.0.12; hierarchical similarity measure based on Euclidean distances and "complete" clustering method).

Quantitative RT-PCR

RNA was extracted using the TRIzol reagent (Invitrogen) protocol as described above. cDNA was generated using the iScript cDNA Synthesis Kit (Bio-Rad) starting with 1 μg of RNA as input in 20 μl of reactions and incubated at 25°C for 5 min, at 46°C for 20 min, and at 95°C for 1 min followed by cooldown to 4°C. qRT-PCR was performed with 10 ng of cDNA per well, in the 384w ViiA 7 System using 1× Power SYBR Green PCR Master Mix (Applied Biosystems), in 10 μl per well. Primers are listed in table S4.

Supplementary Materials

This PDF file includes:

Figs. S1 to S7
Legends for tables S1 to S4

Other Supplementary Material for this manuscript includes the following:

Tables S1 to S4

View/request a protocol for this paper from *Bio-protocol*.

REFERENCES AND NOTES

1. R. R. Goel, M. M. Painter, S. A. Apostolidis, D. Mathew, W. Meng, A. M. Rosenfeld, K. A. Lundgreen, A. Reynaldi, D. S. Khoury, A. Pattekar, S. Gouma, L. Kuri-Cervantes, P. Hicks, S. Dysinger, A. Hicks, H. Sharma, S. Herring, S. Korte, A. E. Baxter, D. A. Oldridge, J. R. Giles, M. E. Weirick, C. M. McAllister, M. Awofolaju, N. Tanenbaum, E. M. Drapeau, J. Dougherty, S. Long, K. D'Andrea, J. T. Hamilton, M. McLaughlin, J. C. Williams, S. Adamski, O. Kuthuru; The UPenn COVID Processing Unit‡, I. Frank, M. R. Betts, L. A. Vella, A. Grifoni, D. Weiskopf, A. Sette, S. E. Hensley, M. P. Davenport, P. Bates, E. T. Luning Prak, A. R. Greenplate, E. J. Wherry, mRNA vaccines induce durable immune memory to SARS-CoV-2 and variants of concern. *Science* **374**, eabm0829 (2021).
2. A. J. Bernal, M. M. Gomes da Silva, D. B. Musungaie, E. Kovalchuk, A. Gonzalez, V. D. Reyes, A. Martín-Quirós, Y. Caraco, A. Williams-Diaz, M. L. Brown, J. Du, A. Pedley, C. Assaid, J. Strizki, J. A. Grobler, H. H. Shamsuddin, R. Tipping, H. Wan, A. Paschke, J. R. Butterton, M. G. Johnson, C. De Anda; MOVe-OUT Study Group, Molnupiravir for oral treatment of covid-19 in nonhospitalized patients. *N. Engl. J. Med.* **386**, 509–520 (2022).
3. I. Wijaya, R. Andhika, I. Huang, A. Purwiga, K. Y. Budiman, M. H. Bashari, L. Reniarti, R. M. A. Roesli, The use of Janus kinase inhibitors in hospitalized patients with COVID-19: Systematic review and meta-analysis. *Clin. Epidemiol. Glob. Health* **11**, 100755 (2021).
4. The RECOVERY Collaborative Group, Dexamethasone in hospitalized patients with Covid-19. *N. Engl. J. Med.* **384**, 693–704 (2021).
5. A. C. Kalil, T. F. Patterson, A. K. Mehta, K. M. Tomashek, C. R. Wolfe, V. Ghazaryan, V. C. Marconi, G. M. Ruiz-Palacios, L. Hsieh, S. Kline, V. Tapson, N. M. Iovine, M. K. Jain, D. A. Sweeney, H. M. el Sahly, A. R. Branche, J. Regalado Pineda, D. C. Lye, U. Sandkovsky, A. F. Luetkemeyer, S. H. Cohen, R. W. Finberg, P. E. H. Jackson, B. Taiwo, C. I. Paules, H. Arguinchona, N. Erdmann, N. Ahuja, M. Frank, M. D. Oh, E. S. Kim, S. Y. Tan, R. A. Mularski, H. Nielsen, P. O. Ponce, B. S. Taylor, L. Larson, N. G. Rouphael, Y. Saklawi, V. D. Cantos, E. R. Ko, J. J. Engemann, A. N. Amin, M. Watanabe, J. Billings, M. C. Elie, R. T. Davey, T. H. Burgess, J. Ferreira, M. Green, M. Makowski, A. Cardoso, S. de Bono, T. Bonnett, M. Proschan, G. A. Deye, W. Dempsey, S. U. Nayak, L. E. Dodd, J. H. Beigel; ACTT-2 Study Group Members, Baricitinib plus remdesivir for hospitalized adults with Covid-19. *N. Engl. J. Med.* **384**, 795–807 (2021).
6. J. L. Schultze, A. C. Aschenbrenner, COVID-19 and the human innate immune system. *Cell* **184**, 1671–1692 (2021).
7. R. L. Chua, S. Lukassen, S. Trump, B. P. Hennig, D. Wendisch, F. Pott, O. Debnath, L. Thürmann, F. Kurth, M. T. Völker, J. Kazmierski, B. Timmermann, S. Twardziok, S. Schneider, F. Machleidt, H. Müller-Redetzky, M. Maier, A. Krannich, S. Schmidt, F. Balzer, J. Liebig, J. Loske, N. Suttorp, J. Eils, N. Ishaque, U. G. Liebert, C. von Kalle, A. Hocke, M. Witzenrath, C. Goffinet, C. Drosten, S. Laudi, I. Lehmann, C. Conrad, L. E. Sander, R. Eils,

COVID-19 severity correlates with airway epithelium-immune cell interactions identified by single-cell analysis. *Nat. Biotechnol.* **38**, 970–979 (2020).
8. T. Kouwaki, T. Nishimura, G. Wang, H. Oshiumi, RIG-I-like receptor-mediated recognition of viral genomic RNA of severe acute respiratory syndrome coronavirus-2 and viral escape from the host innate immune responses. *Front. Immunol.* **12**, 700926 (2021).
9. M. Zheng, R. Karki, E. P. Williams, D. Yang, E. Fitzpatrick, P. Vogel, C. B. Jonsson, T. D. Kanneganti, TLR2 senses the SARS-CoV-2 envelope protein to produce inflammatory cytokines. *Nat. Immunol.* **22**, 829–838 (2021).
10. H. E. Jung, H. K. Lee, Current understanding of the innate control of Toll-like receptors in response to SARS-CoV-2 infection. *Viruses* **13**, 2132 (2021).
11. L. C. Van Eyndhoven, A. Singh, J. Tel, Decoding the dynamics of multilayered stochastic antiviral IFN-I responses. *Trends Immunol.* **42**, 824–839 (2021).
12. U. Rand, U. Hillebrand, S. Sievers, S. Willenberg, M. Köster, H. Hauser, D. Wirth, Uncoupling of the dynamics of host-pathogen interaction uncovers new mechanisms of viral interferon antagonism at the single-cell level. *Nucleic Acids Res.* **42**, e109 (2014).
13. S. Brzostek-Racine, C. Gordon, S. Van Scoy, N. C. Reich, The DNA damage response induces IFN. *J. Immunol.* **187**, 5336–5345 (2011).
14. J. G. Moffat, F. Vincent, J. A. Lee, J. Eder, M. Prunotto, Opportunities and challenges in phenotypic drug discovery: An industry perspective. *Nat. Rev. Drug Discov.* **16**, 531–543 (2017).
15. M. J. Schmitt, C. Company, Y. Dramaretska, I. Barozzi, A. Göhrig, S. Kertalli, M. Großmann, H. Naumann, M. P. Sanchez-Bailon, D. Hulsman, R. Glass, M. Squatrito, M. Serresi, G. Gargiulo, Phenotypic mapping of pathologic cross-talk between glioblastoma and innate immune cells by synthetic genetic tracing. *Cancer Discov.* **11**, 754–777 (2021).
16. M. Serresi, S. Kertalli, L. Li, M. J. Schmitt, Y. Dramaretska, J. Wierikx, D. Hulsman, G. Gargiulo, Functional antagonism of chromatin modulators regulates epithelial-mesenchymal transition. *Sci. Adv.* **7**, eabd7974 (2021).
17. C. Comxpany, M. J. Schmitt, Y. Dramaretska, S. Kertalli, B. Jiang, M. Serresi, I. Barozzi, G. Gargiulo, Logical design of synthetic cis-regulatory DNA for genetic tracing of cell identities and state changes. bioRxiv 2022.11.04.515171 [**Preprint**]. 5 November 2022. https://doi.org/10.1101/2022.11.04.515171.
18. D. Blanco-Melo, B. E. Nilsson-Payant, W. C. Liu, S. Uhl, D. Hoagland, R. Møller, T. X. Jordan, K. Oishi, M. Panis, D. Sachs, T. T. Wang, R. E. Schwartz, J. K. Lim, R. A. Albrecht, B. R. tenOever, Imbalanced host response to SARS-CoV-2 drives development of COVID-19. *Cell* **181**, 1036–1045.e9 (2020).
19. M. M. Lamers, J. Beumer, J. van der Vaart, K. Knoops, J. Puschhof, T. I. Breugem, R. B. G. Ravelli, J. Paul van Schayck, A. Z. Mykytyn, H. Q. Duimel, E. van Donselaar, S. Riesebosch, H. J. H. Kuijpers, D. Schipper, W. J. van de Wetering, M. de Graaf, M. Koopmans, E. Cuppen, P. J. Peters, B. L. Haagmans, H. Clevers, SARS-CoV-2 productively infects human gut enterocytes. *Science* **369**, 50–54 (2020).
20. E. Wyler, K. Mösbauer, V. Franke, A. Diag, L. T. Gottula, R. Arsiè, F. Klironomos, D. Koppstein, K. Hönzke, S. Ayoub, C. Buccitelli, K. Hoffmann, A. Richter, I. Legnini, A. Ivanov, T. Mari, S. del Giudice, J. Papies, S. Praktiknjo, T. F. Meyer, M. A. Müller, D. Niemeyer, A. Hocke, M. Selbach, A. Akalin, N. Rajewsky, C. Drosten, M. Landthaler, Transcriptomic profiling of SARS-CoV-2 infected human cell lines identifies HSP90 as target for COVID-19 therapy. *iScience* **24**, 102151 (2021).
21. W. Emanuel, M. Kirstin, F. Vedran, D. Asija, G. L. Theresa, A. Roberto, K. Filippos, K. David, A. Salah, B. Christopher, R. Anja, L. Ivano, I. Andranik, M. Tommaso, D. G. Simone, P. J. Patrick, M. M. Alexander, N. Daniela, S. Matthias, A. Altuna, R. Nikolaus, D. Christian, L. Markus, Bulk and single-cell gene expression profiling of SARS-CoV-2 infected human cell lines identifies molecular targets for therapeutic intervention. bioRxiv 2020.05.05.079194 [**Preprint**]. 5 May 2020. https://doi.org/10.1101/2020.05.05.079194.
22. V. Hornung, J. Ellegast, S. Kim, K. Brzózka, A. Jung, H. Kato, H. Poeck, S. Akira, K. K. Conzelmann, M. Schlee, S. Endres, G. Hartmann, 5′-Triphosphate RNA is the ligand for RIG-I. *Science* **314**, 994–997 (2006).
23. M. Gentili, J. Kowal, M. Tkach, T. Satoh, X. Lahaye, C. Conrad, M. Boyron, B. Lombard, S. Durand, G. Kroemer, D. Loew, M. Dalod, C. Théry, N. Manel, Transmission of innate immune signaling by packaging of cGAMP in viral particles. *Science* **349**, 1232–1236 (2015).
24. R. Gonsky, R. L. Deem, J. H. Bream, D. H. Lee, H. A. Young, S. R. Targan, Mucosa-specific targets for regulation of IFN-gamma expression: Lamina propria T cells use different cis-elements than peripheral blood T cells to regulate transactivation of IFN-gamma expression. *J. Immunol.* **164**, 1399–1407 (2000).
25. X. Xie, A. Muruato, K. G. Lokugamage, K. Narayanan, X. Zhang, J. Zou, J. Liu, C. Schindewolf, N. E. Bopp, P. V. Aguilar, K. S. Plante, S. C. Weaver, S. Makino, J. W. LeDuc, V. D. Menachery, P. Y. Shi, An infectious cDNA clone of SARS-CoV-2. *Cell Host Microbe* **27**, 841–848.e3 (2020).
26. M. Sato, N. Hata, M. Asagiri, T. Nakaya, T. Taniguchi, N. Tanaka, Positive feedback regulation of type I IFN genes by the IFN-inducible transcription factor IRF-7. *FEBS Lett.* **441**, 106–110 (1998).
27. F. Kok, M. Rosenblatt, M. Teusel, T. Nizharadze, V. Gonçalves Magalhães, C. Dächert, T. Maiwald, A. Vlasov, M. Wäsch, S. Tyufekchieva, K. Hoffmann, G. Damm, D. Seehofer, T. Boettler, M. Binder, J. Timmer, M. Schilling, U. Klingmüller, Disentangling molecular mechanisms regulating sensitization of interferon alpha signal transduction. *Mol. Syst. Biol.* **16**, e8955 (2020).
28. J. Andersen, S. VanScoy, T. F. Cheng, D. Gomez, N. C. Reich, IRF-3-dependent and augmented target genes during viral infection. *Genes Immun.* **9**, 168–175 (2008).
29. F. Rödel, B. Frey, U. Gaipl, L. Keilholz, C. Fournier, K. Manda, H. Schöllnberger, G. Hildebrandt, C. Rödel, Modulation of inflammatory immune reactions by low-dose ionizing radiation: Molecular mechanisms and clinical application. *Curr. Med. Chem.* **19**, 1741–1750 (2012).
30. L. J. M. Bruurs, M. Müller, J. G. Schipper, H. H. Rabouw, S. Boersma, F. J. M. van Kuppeveld, M. E. Tanenbaum, Heterogeneity in viral replication dynamics shapes the antiviral response. bioRxiv 2022.06.08.495262 [**Preprint**]. 8 June 2022. https://doi.org/10.1101/2022.06.08.495262.
31. W. Nicolay, R. Moeller, S. Kahl, F. W. R. Vondran, T. Pietschmann, S. Kunz, G. Gerold, Characterization of RNA sensing pathways in hepatoma cell lines and primary human hepatocytes. *Cells* **10**, 3019 (2021).
32. K. Guo, B. S. Barrett, J. H. Morrison, K. L. Mickens, E. K. Vladar, K. J. Hasenkrug, E. M. Poeschla, M. L. Santiago, Interferon resistance of emerging SARS-CoV-2 variants. *Proc. Natl. Acad. Sci. U.S.A.* **119**, e2203760119 (2022).
33. T. Mao, B. Israelow, C. Lucas, C. B. F. Vogels, M. L. Gomez-Calvo, O. Fedorova, M. I. Breban, B. L. Menasche, H. Dong, M. Linehan; Yale SARS-CoV-2 Genome Surveillance Initiative, T. Alpert, F. B. Anderson, R. Earnest, J. R. Fauver, C. C. Kalinich, K. Munyenyembe, I. M. Ott, M. E. Petrone, J. Rothman, A. E. Watkins, C. B. Wilen, M. L. Landry, N. D. Grubaugh, A. M. Pyle, A. Iwasaki, A stem-loop RNA RIG-I agonist protects against acute and chronic SARS-CoV-2 infection in mice. *J. Exp. Med.* **219**, (2022).
34. J. S. Y. Ho, B. W.-Y. Mok, L. Campisi, T. Jordan, S. Yildiz, S. Parameswaran, J. A. Wayman, N. N. Gaudreault, D. A. Meekins, S. V. Indran, I. Morozov, J. D. Trujillo, Y. S. Fstkchyan, R. Rathnasinghe, Z. Zhu, S. Zheng, N. Zhao, K. White, H. Ray-Jones, V. Malysheva, M. J. Thiecke, S.-Y. Lau, H. Liu, A. J. Zhang, A. C.-Y. Lee, W.-C. Liu, S. Jangra, A. Escalera, T. Aydillo, B. S. Melo, E. Guccione, R. Sebra, E. Shum, J. Bakker, D. A. Kaufman, A. L. Moreira, M. Carossino, U. B. R. Balasuriya, M. Byun, R. A. Albrecht, M. Schotsaert, A. Garcia-Sastre, S. K. Chanda, E. R. Miraldi, A. D. Jeyasekharan, B. R. Ten Oever, M. Spivakov, M. T. Weirauch, S. Heinz, H. Chen, C. Benner, J. A. Richt, I. Marazzi, TOP1 inhibition therapy protects against SARS-CoV-2-induced lethal inflammation. *Cell* **184**, 2618–2632.e17 (2021).
35. A. Rialdi, L. Campisi, N. Zhao, A. C. Lagda, C. Pietzsch, J. S. Y. Ho, L. Martinez-Gil, R. Fenouil, X. Chen, M. Edwards, G. Metreveli, S. Jordan, Z. Peralta, C. Munoz-Fontela, N. Bouvier, M. Merad, J. Jin, M. Weirauch, S. Heinz, C. Benner, H. van Bakel, C. Basler, A. García-Sastre, A. Bukreyev, I. Marazzi, Topoisomerase 1 inhibition suppresses inflammatory genes and protects from death by inflammation. *Science* **352**, eaad7993 (2016).
36. A. Rialdi, J. Hultquist, D. Jimenez-Morales, Z. Peralta, L. Campisi, R. Fenouil, N. Moshkina, Z. Z. Wang, B. Laffleur, R. M. Kaake, M. J. McGregor, K. Haas, E. Pefanis, R. A. Albrecht, L. Pache, S. Chanda, J. Jen, J. Ochando, M. Byun, U. Basu, A. García-Sastre, N. Krogan, H. van Bakel, I. Marazzi, The RNA exosome syncs IAV-RNAPII transcription to promote viral ribogenesis and infectivity. *Cell* **169**, 679–692.e14 (2017).
37. H. Amatullah, I. Fraschilla, S. Digumarthi, J. Huang, F. Adiliaghdam, G. Bonilla, L. P. Wong, M. E. Rivard, C. Beauchamp, V. Mercier, P. Goyette, R. I. Sadreyev, R. M. Anthony, J. D. Rioux, K. L. Jeffrey, Epigenetic reader SP140 loss of function drives Crohn's disease due to uncontrolled macrophage topoisomerases. *Cell* **185**, 3232–3247.e18 (2022).
38. N. Figueiredo, A. Chora, H. Raquel, N. Pejanovic, P. Pereira, B. Hartleben, A. Neves-Costa, C. Moita, D. Pedroso, A. Pinto, S. Marques, H. Faridi, P. Costa, R. Gozzelino, J. L. Zhao, M. P. Soares, M. Gama-Carvalho, J. Martinez, Q. Zhang, G. Döring, M. Grompe, J. P. Simas, T. B. Huber, D. Baltimore, V. Gupta, D. R. Green, J. A. Ferreira, L. F. Moita, Anthracyclines induce DNA damage response-mediated protection against severe sepsis. *Immunity* **39**, 874–884 (2013).
39. J. Stebbing, G. Sánchez Nievas, M. Falcone, S. Youhanna, P. Richardson, S. Ottaviani, J. X. Shen, C. Sommerauer, G. Tiseo, L. Ghiadoni, A. Virdis, F. Monzani, L. R. Rizos, F. Forfori, A. Avendaño Céspedes, S. de Marco, L. Carrozzi, F. Lena, P. M. Sánchez-Jurado, L. G. Lacerenza, N. Cesira, D. Caldevilla Bernardo, A. Perrella, L. Niccoli, L. S. Méndez, D. Matarrese, D. Goletti, Y. J. Tan, V. Monteil, G. Dranitsaris, F. Cantini, A. Farcomeni, S. Dutta, S. K. Burley, H. Zhang, M. Pistello, W. Li, M. M. Romero, F. Andrés Pretel, R. S. Simón-Talero, R. García-Molina, C. Kutter, J. H. Felce, Z. F. Nizami, A. G. Miklosi, J. M. Penninger, F. Menichetti, A. Mirazimi, P. Abizanda, V. M. Lauschke, JAK inhibition reduces SARS-CoV-2 liver infectivity and modulates inflammatory responses to reduce morbidity and mortality. *Sci. Adv.* **7**, eabe4724 (2021).
40. A. C. Kalil, A. K. Mehta, T. F. Patterson, N. Erdmann, C. A. Gomez, M. K. Jain, C. R. Wolfe, G. M. Ruiz-Palacios, S. Kline, J. Regalado Pineda, A. F. Luetkemeyer, M. S. Harkins, P. E. H. Jackson, N. M. Iovine, V. F. Tapson, M. D. Oh, J. A. Whitaker, R. A. Mularski, C. I. Paules, D. Ince, J. Takasaki, D. A. Sweeney, U. Sandkovsky, D. L. Wyles, E. Hohmann, K. A. Grimes,

R. Grossberg, M. Laguio-Vila, A. A. Lambert, D. Lopez de Castilla, E. S. Kim, L. A. Larson, C. R. Wan, J. J. Traenkner, P. O. Ponce, J. E. Patterson, P. A. Goepfert, T. A. Sofarelli, S. Mocherla, E. R. Ko, A. Ponce de Leon, S. B. Doernberg, R. L. Atmar, R. C. Maves, F. Dangond, J. Ferreira, M. Green, M. Makowski, T. Bonnett, T. Beresnev, V. Ghazaryan, W. Dempsey, S. U. Nayak, L. Dodd, K. M. Tomashek, J. H. Beigel, A. Hewlett, B. S. Taylor, J. E. Bowling, R. C. Serrano, N. G. Rouphael, Z. Wiley, V. K. Phadke, L. Certain, H. N. Imlay, J. J. Engemann, E. B. Walter, J. Meisner, S. Rajme, J. Billings, H. Kim, J. A. Martinez-Orozco, N. Bautista Felix, S. T. Elmor, L. R. Bristow, G. Mertz, N. Sosa, T. D. Bell, M. J. West, M. C. Elie-Turenne, J. Grein, F. Sutterwala, P. Gyun Choe, C. Kyung Kang, H. M. el Sahly, K. S. Rhie, R. H. Hussein, P. L. Winokur, A. Mikami, S. Saito, C. A. Benson, K. McConnell, M. Berhe, E. Dishner, M. G. Frank, E. Sarcone, P. C. B. Crouch, H. Jang, N. Jilg, K. Perez, C. Janak, V. D. Cantos, P. A. Rebolledo, J. Gharbin, B. S. Zingman, P. F. Riska, A. R. Falsey, E. E. Walsh, A. R. Branche, H. Arguinchona, C. Arguinchona, J. W. van Winkle, D. F. Zea, J. Jung, K. H. Song, H. B. Kim, J. Dwyer, E. Bainbridge, D. C. Hostler, J. M. Hostler, B. T. Shahan, L. Hsieh, A. N. Amin, M. Watanabe, W. R. Short, P. Tebas, J. T. Baron, N. Ahuja, E. Ling, M. Go, O. O. Yang, J. Ahn, R. Arias, R. R. Rapaka, F. A. Hubbard, J. D. Campbell, S. H. Cohen, G. R. Thompson 3rd, M. Chakrabarty, S. N. Taylor, N. Masri, A. Lacour, T. Lee, T. Lalani, D. A. Lindholm, A. E. Markelz, K. Mende, C. J. Colombo, C. Schofield, R. E. Colombo, F. Guirgis, M. Holodniy, A. Chary, M. Bessesen, N. A. Hynes, L. M. Sauer, V. C. Marconi, A. Moanna, T. Harrison, D. C. Lye, S. W. X. Ong, P. Ying Chia, N. Huprikar, A. Ganesan, C. Madar, R. M. Novak, A. Wendrow, S. A. Borgetti, S. L. George, D. F. Hoft, J. D. Brien, S. L. F. McLellan, C. Levine, J. Nock, S. Yen Tan, H. Shafi, J. M. F. Chien, K. Candiotti, R. W. Finberg, J. P. Wang, M. Wessolossky, G. C. Utz, S. E. Chambers, D. S. Stephens, T. H. Burgess, J. Rozman, Y. Hyvert, A. Seitzinger, A. Osinusi, H. Cao, K. K. Chung, T. M. Conrad, K. Cross, J. A. el-Khorazaty, H. Hill, S. Pettibone, M. R. Wierzbicki, N. Gettinger, T. Engel, T. Lewis, J. Wang, G. A. Deye, E. Nomicos, R. Pikaart-Tautges, M. Elsafy, R. Jurao, H. Koo, M. Proschan, R. Davey, T. Yokum, J. Arega, R. Florese, Efficacy of interferon beta-1a plus remdesivir compared with remdesivir alone in hospitalised adults with COVID-19: A double-bind, randomised, placebo-controlled, phase 3 trial. *Lancet Respir. Med.* **9**, 1365–1376 (2021).

41. A. Piras, V. Venuti, A. D'Aviero, D. Cusumano, S. Pergolizzi, A. Daidone, L. Boldrini, Covid-19 and radiotherapy: A systematic review after 2 years of pandemic. *Clin. Transl. Imaging* **10**, 611–630 (2022).
42. S. R. Pandey, S. Adhikari Yadav, S. Gautam, K. Giri, A. Devkota, S. Shrestha, S. Bhandari, S. Baniya, B. Adhikari, B. Adhikari, S. Neupane, J. Bhandari, Effectiveness of low-dose radiation therapy in COVID-19 patients globally: A systematic review. *F1000Res.* **11**, 62 (2022).
43. S. Lee, Y. Yu, J. Trimpert, F. Benthani, M. Mairhofer, P. Richter-Pechanska, E. Wyler, D. Belenki, S. Kaltenbrunner, M. Pammer, L. Kausche, T. C. Firsching, K. Dietert, M. Schotsaert, C. Martínez-Romero, G. Singh, S. Kunz, D. Niemeyer, R. Ghanem, H. J. F. Salzer, C. Paar, M. Mülleder, M. Uccellini, E. G. Michaelis, A. Khan, A. Lau, M. Schönlein, A. Habringer, J. Tomasits, J. M. Adler, S. Kimeswenger, A. D. Gruber, W. Hoetzenecker, H. Steinkellner, B. Purfürst, R. Motz, F. D. Pierro, B. Lamprecht, N. Osterrieder, M. Landthaler, C. Drosten, A. García-Sastre, R. Langer, M. Ralser, R. Eils, M. Reimann, D. N. Y. Fan, C. A. Schmitt, Virus-induced senescence is driver and therapeutic target in COVID-19. *Nature* **599**, 283–289 (2021).
44. P. Datlinger, A. F. Rendeiro, T. Boenke, M. Senekowitsch, T. Krausgruber, D. Barreca, C. Bock, Ultra-high-throughput single-cell RNA sequencing and perturbation screening with combinatorial fluidic indexing. *Nat. Methods* **18**, 635–642 (2021).
45. D. Alpern, V. Gardeux, J. Russeil, B. Mangeat, A. C. A. Meireles-Filho, R. Breysse, D. Hacker, B. Deplancke, BRB-seq: Ultra-affordable high-throughput transcriptomics enabled by bulk RNA barcoding and sequencing. *Genome Biol* **20**, 71 (2019).

Acknowledgments: We are grateful to E. von Weizsaecker (Ascenion) for connecting the Gargiulo and Čičin-Šain laboratories. We are also grateful to L. Li, H. Naumann, J. Eberle, and the MDC FACS (H.-P. Rahn) and Genomics (T. Borodina) technology platform for technical support. We also thank E. Wyler and M. Landthaler for timely sharing scRNA-seq data and A. Aguzzi for comments. B.J., C.C., M.J.S., and Y.D. are graduate students at Charité and Humboldt University. pscALPSpuro-HsACE2 (human) was a gift from J. Luban (Addgene, plasmid #158081). The MCA peptide-based ACE2 enzyme activity assay was a gift from M. Lebedin and K. de la Rosa. The plasmids generated in this study can be provided by G.G. pending a standard material transfer agreement (see Data and materials availability). **Funding:** The G.G. laboratory acknowledges funding from MDC, BIH, Helmholtz (VH-NG-1153), and ERC (714922). **Author contributions:** Conceptualization: G.G. Methodology: B.J., M.J.S., C.C., M.S., M.G., and U.R. Investigation: G.G., B.J., M.J.S., C.C., M.S., M.G., U.R., and Y.D. Visualization: B.J., M.J.S., and G.G. Supervision: G.G. and L.Č.-Š. Writing—original draft: G.G. Writing—review and editing: G.G., B.J., M.J.S., C.C., M.S., U.R., L.Č.-Š., and Y.D. **Competing interests:** G.G. reports a patent for EP18192715 applied for by Max-Delbrück-Center for Molecular Medicine (MDC), Robert-Rössle-Str. 10, 13092 Berlin, Germany. The other authors declare that they have no competing interests. **Data and materials availability:** All data needed to evaluate the conclusions in the paper are present in the paper and/or the Supplementary Materials. RNA-seq data generated in this study are made available from GEO (series GSE226667). The reporters will be made available through standard MTA via plasmid repositories (e.g., Addgene).

Submitted 4 November 2022
Accepted 17 May 2023
Published 21 June 2023
10.1126/sciadv.adf4975

ScienceAdvances

Pharmacological modulators of epithelial immunity uncovered by synthetic genetic tracing of SARS-CoV-2 infection responses

Ben Jiang, Matthias Jrgen Schmitt, Ulfert Rand, Carlos Company, Yuliia Dramaretska, Melanie Grossmann, Michela Serresi, Luka iin-ain, and Gaetano Gargiulo

Sci. Adv., **9** (25), eadf4975.
DOI: 10.1126/sciadv.adf4975